A new proposal to the Jefferson Lab Program Advisory Committee (PAC34)

Precision Measurement of the Neutron Magnetic Form Factor up to $Q^2 = 18.0$ $(GeV/c)^2$ by the Ratio Method

F. Benmokhtar, G.B. Franklin, B. Quinn (spokesperson), R. Schumacher
Carnegie Mellon University, Pittsburgh, PA 15213

A. Camsonne, J.P. Chen, E. Chudakov, C. DeJager,
P. Degtyarenko, J. Gomez, O. Hansen, D. W. Higinbotham,
M. Jones, J. LeRose, R. Michaels, S. Nanda, A. Saha, V. Sulkosky,
B. Wojtsekhowski (spokesperson and contact person)
Thomas Jefferson National Accelerator Facility, Newport News, VA 23606

L. El Fassi, R. Gilman (spokesperson), G. Kumbartzki, R. Ransome, E. Schulte
Rutgers University, Piscataway, NJ 08854

T. Averett, C.F. Perdrisat, L.P. Pentchev
College of William and Mary

E. Cisbani, F. Cusanno, F. Garibaldi,
S. Frullani, G. M. Urciuoli, M. Iodice, M.L. Magliozzi
INFN, Rome, Italy

H. Baghdasaryan, G. Cates, D. Day, N. Kalantarians, R. Lindgren, N. Liyanage,
V. Nelyubin, B. E. Norum, K. D. Paschke, S. Riordan, X. Zheng
University of Virginia, Charlottesville, VA 22901

W. Brooks
Universidad Tecnica Federico Santa Maria, Valparaiso, Chile

V. Punjabi, M. Khandaker, F. Wesselmann
Norfolk State University

W. Boeglin, P. Markowitz, J. Reinhold
Florida International University, Fl

J. Annand, D. Hamilton, D. Ireland, R. Kaiser, K. Livingston,
I. MacGregor, B. Seitz, and G. Rosner
University of Glasgow, Glasgow, Scotland

D. Nikolenko, I. Rachek, Yu. Shestakov
Budker Institute, Novosibirsk, Russia

R. De Leo, L. La Gamba, S. Marrone, E. Nappi
INFN, Bari, Italy

M. Mihovilovič, M. Potokar, S. Širca
Jožef Stefan Institute and Dept. of Physics, University of Ljubljana, Slovenia

J. Gilfoyle
University of Richmond, Richmond, VA

J. Lichtenstadt, I. Pomerantz, E. Piasetzky, G. Ron
Tel Aviv University, Israel

A. Glamazdin
Kharkov Institute of Physics and Technology, Kharkov 310077, Ukraine

J. Calarco, K. Slifer
University of New Hampshire, Durham, NH 03824

B. Vlahovic
North Carolina Central University, Durham, NC 03824

A. Sarty
Saint Mary's University, Nova Scotia, Canada B3H 3C3

K. Aniol and D. J. Magaziotis
Cal State University, Los Angeles, CA 90032

S. Abrahamyan, S. Mayilyan, A. Shahinyan, H. Voskanyan
Yerevan Physics Institute, Yerevan, Armenia

and
The Hall A Collaboration

December 15, 2008

Abstract

We propose to make a high-precision measurement of the neutron's magnetic form factor, G_M^n, at nine kinematic points: Q^2 = 3.5, 4.5, 6.5, 8.5, 10., 12., 13.5, 16. and 18.0 (GeV/c)^2. Little data on G_M^n exists in this kinematic range and the existing data have large systematic uncertainties. In the proposed experiment, systematic errors are greatly reduced by the use of the "ratio" method in which G_M^n is extracted from the ratio of neutron-coincident to proton-coincident quasi-elastic electron scattering from the deuteron. The experiment would be performed in Hall A using the BigBite spectrometer to detect the scattered electrons and the BigHAND to detect both neutrons and protons. A large aperture dipole magnet on the nucleon flight path will greatly enhance particle identification by slightly deflecting the protons. Calibration reactions will be used to produce tagged neutrons and protons at essentially the same momentum as the quasi-elastic nucleons. The efficiency of BigHAND is expected to be high and stable and to be well calibrated. Projected systematic errors on the measured ratio of cross sections vary from under 2% to 5% (1.% to 2.5% on the ratio of the magnetic form factor to that of the proton). Statistical errors are projected to be similar, or smaller. This proposal overlaps and significantly extends the kinematics range of the already approved 12 GeV CLAS proposal, E12-07-104, which predicts similar uncertainties up to 13.5 (GeV/c)^2. The present proposal includes measurements at Q^2 beyond the range of that experiment and will have significantly greater statistics for the highest-Q^2 points covered by E12-07-104. We request a total of 48.5 days divided among four beam energies, 4.4, 6.6, 8.8 and 11. GeV.

Contents

1 Introduction

The elastic form factors probe the four-current distributions of the nucleons, fundamental quantities that provide one of the best opportunities to test our understanding of nucleon structure. A number of theoretical techniques exist to describe the nucleon's electromagnetic structure, including quark models, perturbative Quantum Chromo-Dynamics (pQCD), lattice QCD, effective field theories, vector-meson dominance (VMD) models, etc. Each at present has limitations, and its validity must be confirmed by experiment. In the examples given,

- quark models, as constructed, are phenomenological with no firm basis in QCD,
- pQCD is limited to high four-momentum transfer, and it is unknown at what momentum transfer it becomes valid,
- lattice QCD is presently limited, by computational requirements, to describing the isovector (proton minus neutron) form factors, since the effects of disconnected quark lines largely cancel in these,
- effective field theories are limited to small momentum transfer, and
- VMD models are constructed as fits to the existing data base.

Experimentally, the nucleon electromagnetic form factors are a central part of the Jefferson Lab 12 GeV program, and it is desirable to measure all four nucleon form factors over the widest possible Q^2 range, to similar precision. This goal is particularly motivated so that one can construct the isovector form factors for comparison with lattice calculations.

In the one-photon approximation the cross section for scattering of electrons from a spin-$\frac{1}{2}$ target can be written as

$$\frac{d\sigma}{d\Omega} = \eta \frac{\sigma_{\rm Mott}}{1+\tau} \left((G_E)^2 + \frac{\tau}{\epsilon} (G_M)^2 \right)$$

where

- $\eta = \frac{1}{1+2\frac{E}{M_N}\sin^2(\theta/2)}$ is the recoil factor
- $\epsilon = (1 + \vec{q}^2/Q^2 \tan^2(\theta/2))^{-1} = (1 + 2(1+\tau)\tan^2(\theta/2))^{-1}$ is the longitudinal polarization of the virtual photon,
- $\tau = Q^2/4M_N^2$, and
- $G_E(Q^2)$ and $G_M(Q^2)$ are the Sachs Electric and Magnetic form factors.

Alternately, the helicity conserving F_1 and helicity nonconserving F_2 form factors can be written as simple linear combinations of the electric G_E and magnetic G_M form factors. The measurement of these form factors for the proton and neutron probes their electromagnetic structures.

Little is known of the neutron's magnetic form factor, $\mathrm{G_M^n}$, (and less of its electric form factor) for $Q^2 > 4$ (GeV/c)^2. *We propose to make several high precision measurements of G_M^n in the range $4.5 < Q^2 < 18.0$ (GeV/c)^2, the largest Q^2 proposed measurements of G_M^n to date.*

Since the form factors are functions only of Q^2, they may be separated by the Rosenbluth technique, making cross section measurements at the same Q^2 but different ϵ to obtain different linear

combinations. The apparent failure of this technique in extraction of G_E^p at $Q^2 > 1$ (GeV/c)^2 (as revealed by the recoil polarization method [2,3]) may indicate a failure of the one-photon exchange approximation [4]. This does not invalidate the form given above, however. It just underscores the fact that the corrections may be non-negligible and may become important particularly when trying to separate a small contribution from a larger one. This consideration does not present a great problem when trying to extract the magnetic form factor of the neutron since the electric form factor is generally much smaller, at least at low Q^2.

These Sachs form factors are trivially related to the Dirac and Pauli form factors, F_1 and F_2, respectively, which are the coefficients of the helicity-conserving and -nonconserving currents to which the photon can couple. Non-relativistically the Sachs form factors can be interpreted as the Fourier transforms of the charge and current distributions to which the photon couples in the target. No such simple interpretation is available at higher Q^2. The electric form factor at any Q^2 can still be related to the Fourier transform in the Breit frame. But since the Breit frame is a different frame for each Q^2, this relationship cannot be inverted to extract a charge distribution without a prescription for boosting the nucleon. Recent work [5] by Miller offers an interpretation of the infinite-momentum frame charge density of the nucleon as a function of impact parameter in terms of the Dirac form factor, $F_1 = (G_e + \tau G_m)/(1 + \tau)$. Interestingly, this implies that knowledge of the *magnetic* form factor of the neutron is important to the understanding of its charge distribution. Furthermore, Miller concludes that the neutron charge distribution is negative for small impact parameter, which contrasts, at least naïvely, with the long-standing belief that the neutron charge distribution is positive at the center. A positive central charge distribution is in accordance with intuitive models – for example, the neutron charge distribution reflects a virtual $p\pi^-$ pair, with the more massive proton closer to the center of mass. The interest in understanding the charge distribution is reflected by the appearance of a figure indicating the positive central charge distribution in the recent Nuclear Physics long Range Plan.

In the approximation that the strange quark does not contribute to the electromagnetic structure of the nucleon, the form factors can be combined [6–8] to extract information about the contributions of individual quark flavors to the electromagnetic structure of the nucleon. Assuming isospin symmetry, the up-quark distribution of the proton is identical to the down-quark distribution of the neutron and *vice versa*. Since the electromagnetic couplings to the individual quarks are known (and the coupling to gluons vanishes) the electric or magnetic form factor of each nucleon can be written as a linear combination of the electric and magnetic form factors of the two quark flavors. Combining measurements on the neutron and proton then allows direct extraction of the "up" form factor (including contributions from u and $\bar{u}$ quarks from the sea, as well as valence quarks) and the "down" form factor (also composed of all d and $\bar{d}$ contributions). In particular, improved measurements of the neutron's magnetic form factor can be combined with existing measurements of the proton's magnetic form factor to allow extraction of the "up-magnetic form factor" and "down-magnetic form factor". If, on the other hand, the contribution of strange quarks is *not* negligible, then the measurement of the neutron form factors would be critical to allowing the strange contribution to be measured. (At present, however, there are no plans to measure strange form factors in the Q^2 range in which we propose to measure.)

The form factors are pivotal as the meeting place between theory and experiment. Calculations of nucleon structure (as opposed to parameterizations of form factors) can be tested by their ability to predict the experimentally accessible information on nucleon structure reflected in the form factors. (Of course, polarization observables and structure functions will also be relevant.) In par-

ticular, lattice QCD predictions will eventually have the capability to make meaningful predictions of hadronic structure. Form factors of the proton and neutron will present important tests of those predictions.

A great deal of experimental and theoretical effort [9–11] is being expended on an ambitious effort to greatly expand the knowledge of nucleon structure by determining the generalized parton distributions. Measurement of form factors plays an important role in that effort since the form factors set the values of sum rules which the generalized parton distributions must obey.

The neutron's form factors are more difficult to measure, of course, because there is no free-neutron target. Spin-asymmetry techniques have been used in extracting the tiny electric form factor of the neutron [12–18] and also in measuring the magnetic [19–21] form factor, particularly at low Q^2. Generally at high Q^2, however, quasielastic scattering from the deuteron has been used [22–37] to extract G_M^n. This is based on the fact that the deuteron is a loosely coupled system, so high-Q^2 quasi-elastic scattering can be viewed as the sum of scattering from a proton target and scattering from a neutron target. This simple picture is complicated only slightly by the fact that the targets are not at rest but are moving with the "Fermi motion" intrinsic to the deuteron's wave-function.

Several techniques have been used to try to isolate the electron-neutron scattering of interest. In the "proton-subtraction" technique [22–27] single-arm quasi-elastic electron scattering from the deuteron is measured. This is combined with a measurement of single-arm elastic scattering from the proton. An attempt is made to fold in the expected effects of Fermi motion to simulate the expected contribution of the proton in the measured quasi-elastic spectrum. This is then subtracted and the remainder is interpreted as a measure of quasi-elastic electron scattering off the neutron from which the (almost purely magnetic) form factor can be determined. This technique tends to suffer from the error-propagation problems intrinsic to subtraction of two large numbers. At low Q^2 the proton electric form factor dominates (and the proton magnetic form factor is never small compared to the neutron's). At high Q^2 inelastic background becomes a serious problem, to the extent that the quasi-elastic "peak" may not be visible, even as a shoulder on the background peak. Because these are single-arm measurements, no other information is available with which to selectively reject background events.

The "proton-tagging" technique [28, 29] is a partial-coincidence method which takes advantage of the fact that protons are easier to detect than neutrons. In that technique quasi-elastic electron scattering is measured with an additional charged-particle detector centered around the direction of the momentum-transfer vector, $\vec{q}$. If no proton is detected, the event is ascribed to scattering from the neutron. This technique generally requires substantial theory-based corrections to account for the tail of the Fermi-motion which would cause a recoil proton to miss the charged-particle detector (or cause a spectator proton to hit it). Again, since the neutron is not detected, no cuts can be applied to selectively reject inelastic background events.

We propose to use the "ratio-method" [38] which is discussed in detail in the next section. It relies on measurement of both the recoil protons and recoil neutrons [30–37]. Inelastic background is substantially suppressed by even a crude nucleon-coincidence requirement. As will be seen in simulations presented in section 9, precise measurement of the final-nucleon direction permits the use of cuts which further reduce inelastic background down to manageable levels, even at the highest Q^2. If the particle detection, particularly the neutron detection is well understood, this technique is subject to the smallest systematic errors as it enjoys substantial cancellation of many sources of systematic error which plague other techniques.

There are relatively few measurements of G_M^n beyond $Q^2 = 1$ (GeV/c)^2. The few published measurements in the range $1 < Q^2 < 4.5$ (GeV/c)^2 (shown in Fig. 1) have been eclipsed, both in number of points and in precision, by the recent CLAS data [37, 39] of Lachniet. These (not yet published) data are shown in Fig. 1 as the blue points. Several of the proposers of the present experiment played key roles in the CLAS experiment (Quinn, Brooks and Gilfoyle). The ratio-method was used for those measurements and will be used in the proposed experiment.

In the figure, the value of G_M^n is divided by the 'scaled dipole'. The dipole is a vector-meson-dominance-inspired empirical parameterization of the proton's electric form factor: $G_E^p \approx G_D = (1 + Q^2/.71 \text{ (GeV/c)}^2)^{-2}$. This appeared to be a good approximation for G_E^p over a large Q^2 range until recent recoil-polarization measurements [2, 3]) showed that G_E^p actually fell rapidly below the dipole form for $Q^2 > 1$ (GeV/c)^2. The scaling approximation hypothesizes that $G_M^p \approx \mu_p G_D$ and $G_M^n \approx \mu_n G_D$. The CLAS data show that the 'scaled dipole' is a surprisingly good approximation for G_M^n out to $Q^2 \approx 4.5$ (GeV/c)^2.

Beyond $Q^2 = 4.5$ (GeV/c)^2 there are only a few points, with large errors. The points plotted in green in Fig. 1 are SLAC measurements [26] made using the "proton-subtraction" technique. While these points have relatively large errors, they point to a trend which is not seen in the CLAS data. This makes it particularly interesting to investigate the behavior of G_M^n in the range $Q^2 > 4$ (GeV/c)^2 with a measurement which is independent of either of those shown in Fig. 1. A similar plot is presented at the end of the proposal, with the projected errors of the proposed measurement superimposed.

2 Technique

We propose to use the "ratio method" [38] to determine G_M^n from quasi-elastic electron scattering on the deuteron for $3.5 < Q^2 < 18$ (GeV/c)^2. This method is far less sensitive to systematic errors than the "proton-subtraction" or "proton-tagging" techniques.

Use of the "ratio method" requires the measurement of both neutron-tagged, d(e,e′n), and proton-tagged, d(e,e′p), quasi-elastic scattering from the deuteron. Simultaneous measurements of both these reactions provides a substantial reduction of systematic error because numerous experimental uncertainties cancel in forming the ratio:

$$R'' = \frac{\frac{d\sigma}{d\Omega}\big|_{\text{d(e,e'n)}}}{\frac{d\sigma}{d\Omega}\big|_{\text{d(e,e'p)}}} \tag{1}$$

This is insensitive, for example, to target thickness, beam intensity, deadtime, electron trigger efficiency, electron acceptance, and the detection and reconstruction efficiency for the scattered electron track.

With a small and accurately-calculable nuclear correction, ϵ_{nuc}, this measured ratio of quasi-elastic cross sections can be used to determine the ratio of the elastic cross sections:

$$R' = \frac{\frac{d\sigma}{d\Omega}\big|_{\text{n(e,e')}}}{\frac{d\sigma}{d\Omega}\big|_{\text{p(e,e')}}} = \frac{R''}{1 + \epsilon_{\text{nuc}}}$$

Because of final-state interactions and other nuclear effects, there would be substantial corrections to the naïve assumption that the coincident quasi-elastic cross section is equal to the cross section for

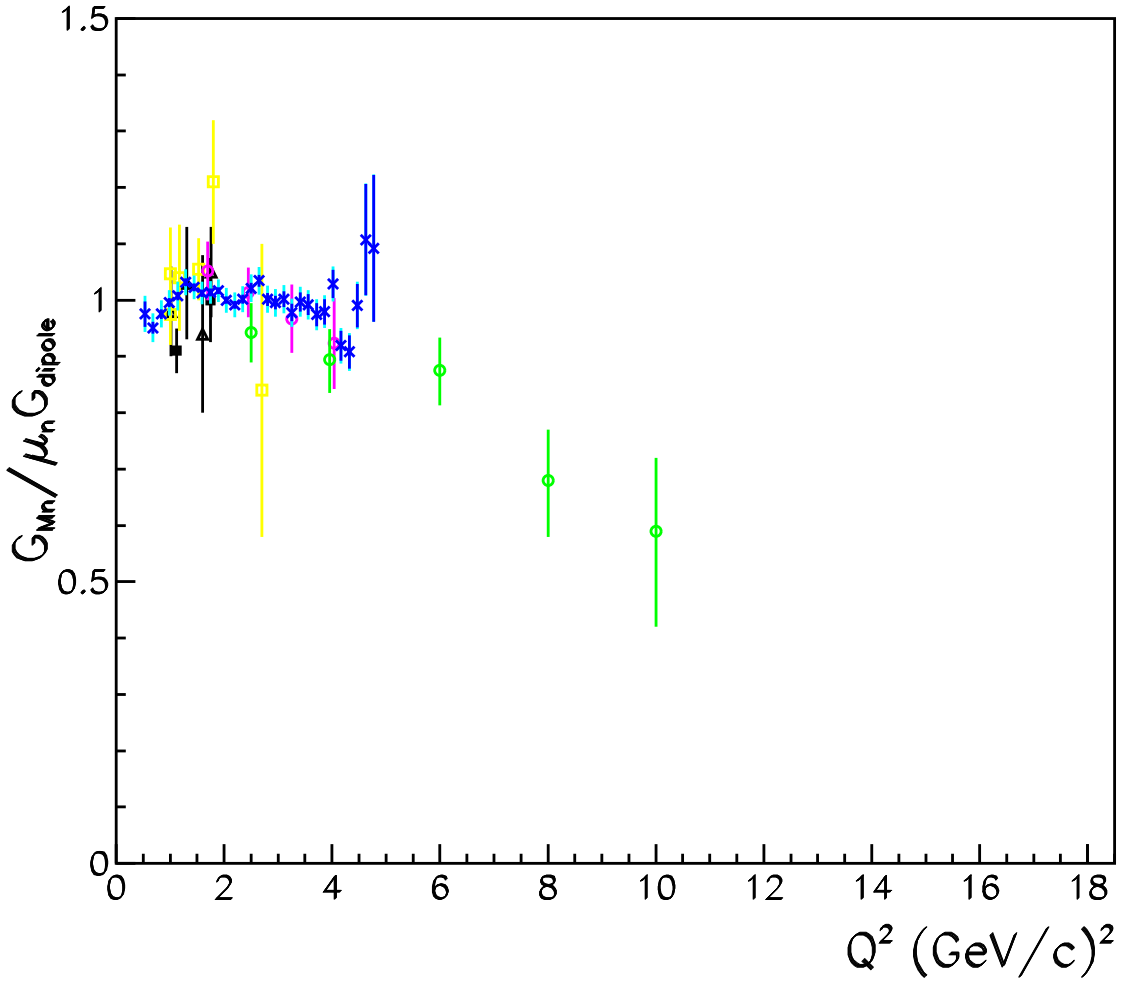

Figure 1: Existing data on G_M^n in $Q^2 > 1$ (GeV/c)^2 range are plotted as ratio to scaled dipole approximation. Blue points are from CLAS e5 run [37,39]. Dark blue lines show the statistical error while light blue lines are the quadrature sum of statistical and systematic errors. Green circle [26] and magenta circle [27] points are from SLAC. Older data are shown as yellow squared [31], solid squares [29], and hollow triangles [25]. Some points have been slightly displaced horizontally to avoid overlap.

elastic scattering from the free nucleon. Further, these corrections would depend upon the fraction of the quasi-elastic peak which is integrated. A great advantage of the ratio method (with a deuteron target) lies in the fact that these corrections are almost identical for the case of the neutron and the proton and so they cancel almost completely in the ratio. The small surviving correction, $\epsilon_{\rm nuc}$, to the ratio arises due to small effects such as the neutron-proton mass difference. Figure 2 shows detailed calculations [41] by Arenhövel of the correction factor required in calculating the ratio of the nucleon elastic cross sections from the ratio of the integrated nucleon-tagged quasi-elastic cross sections. Here θ_{pq} is the angle between the struck nucleon's final momentum vector ($\vec{p}$) and the momentum-transfer vector ($\vec{q}$). Final state interaction effects are minimized by putting a tight cut on θ_{pq} (i.e. requiring that the nucleon actually recoil in the direction which would be expected in the absence of Fermi motion and final state interactions). It will be seen below that the region of interest in the present proposal has $\theta_{pq} < 3$ degrees. Even at $Q^2 = 1.2$ (GeV/c)^2 the correction is seen to be less than 1%. For higher Q^2 up to 5 (GeV/c)^2 calculations of the nuclear correction have been made [37, 39] using a model [42] which applies Glauber theory to model the final-state interactions. Again, the corrections for the neutron and proton are almost identical and cancel in the ratio. The residual correction on the ratio $\epsilon_{\rm nuc}$ was found to be under 0.1%. The corrections are expected to be very small and calculable in the range of interest here. This correction is expected to contribute negligibly to the systematic error of the measurement.

Writing R' in terms of neutron form factors,

$$R' = \frac{\eta \frac{\sigma_{\rm Mott}}{1+\tau} \left((G_E^n)^2 + \frac{\tau}{\epsilon} (G_M^n)^2 \right)}{\frac{d\sigma}{d\Omega}\big|_{\rm p(e,e')}}$$

where η, ϵ, and τ are defined above.

From this, then, can be extracted the ratio of interest,

$$R = R' - \frac{\eta \frac{\sigma_{\rm Mott}}{1+\tau} (G_E^n)^2}{\frac{d\sigma}{d\Omega}\big|_{\rm p(e,e')}} = \frac{\eta \sigma_{\rm Mott} \frac{\tau/\epsilon}{1+\tau} (G_M^n)^2}{\frac{d\sigma}{d\Omega}\big|_{\rm p(e,e')}} \tag{2}$$

The term subtracted to extract R from R' will be small ($\approx 1\%$ at most, and much less at high Q^2) if $\mathrm{G_E^n}$ follows the form of the Galster parameterization. In section 11 we will allow for an error of 100% of Galster (at low Q^2) up to 400% of Galster (at high Q^2) and find that this correction still does not cause unacceptable systematic errors. A measurement of $\mathrm{G_E^n}$ up to $Q^2 = 10$ (GeV/c)^2 is planned [40] in a time-frame which will make it useful for analysis of results from this measurement.

This measurement of R then allows $\mathrm{G_M^n}$ to be determined, given just the proton's elastic cross-section at the corresponding kinematics. It may be noted that, because R is proportional to the square of $\mathrm{G_M^n}$, the fractional error on $\mathrm{G_M^n}$ will actually be only half of the fractional error on R. Since the quantity of greatest interest is $\mathrm{G_M^n}$, it is conventional to report the expected size of the errors on $\mathrm{G_M^n}$. However, the experiment will actually be a direct measurement of R'' (from which R is inferred with small corrections, as described above). This distinction is significant only in that present uncertainties on the proton's form factors (and cross section) do not actually imply systematic errors on the quantity being measured, R'' (or R). Subsequent improvements in the determination of the proton cross section, at the kinematics of interest, can be combined retrospectively with the results for R from this measurement to obtain improved values for $\mathrm{G_M^n}$. There would be no need to repeat the analysis of this experiment to incorporate new proton measurements.

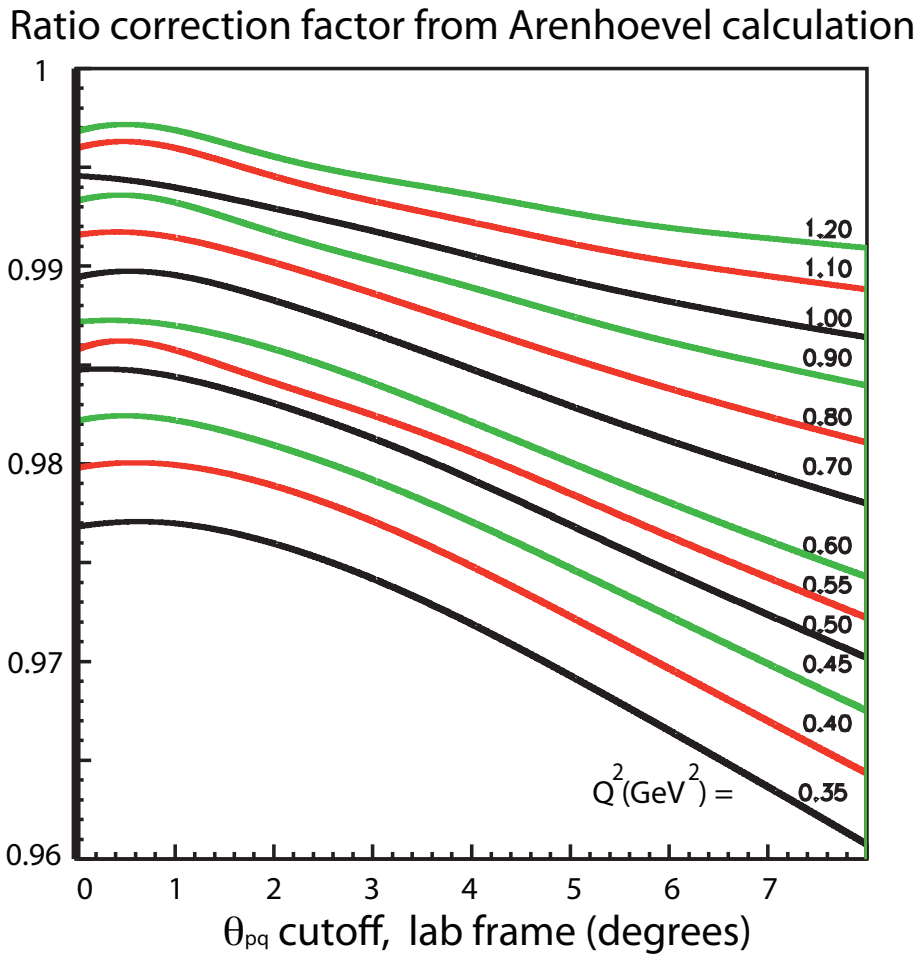

Figure 2: Arenhövel predictions for (low Q^2) nuclear corrections (including FSI) as a function of the maximum accepted value of θ_{pq}. The required correction is seen to be small for tight cuts on θ_{pq} and to *decrease* with increasing Q^2.

Table 1: Kinematics of proposed measurements

Q^2 $(GeV/c)^2$	E_{beam} (GeV)	θ_e	θ_N	E' (GeV)	P_N (GeV/c)
3.5	4.4	32.5°	31.1°	2.5	2.6
4.5	4.4	41.9°	24.7°	2.0	3.2
6.	4.4	64.3°	15.6°	1.2	4.0
8.5	6.6	46.5°	16.2°	2.1	5.4
10.	8.8	33.3°	17.9°	3.5	6.2
12.	8.8	44.2°	13.3°	2.4	7.3
13.5	8.8	58.5°	9.8°	1.6	8.1
16.	11.	45.1°	10.7°	2.5	9.4
18.	11.	65.2°	7.0°	1.4	10.5

Similarly, since the proton cross section is dominated by G_M^p for these kinematics, the ratio of formfactors, G_M^n/G_M^p can be cleanly extracted from the data. In many ways this ratio is more fundamental than G_M^n, lending itself to direct comparison to theoretical predictions. Extraction of this ratio does not suffer from a systematic error due to uncertainties in proton cross section measurements. Like G_M^n, this ratio enjoys a factor of two reduction in the fractional error compared to R.

3 Proposed Kinematics

The kinematic points at which we propose to measure are shown in Table 1. The lowest-Q^2 points will overlap with existing CLAS measurements while the highest-Q^2 points will greatly extend the range in which G_M^n is known with high precision

While the scattered electron energy is relatively constant (mostly near 1 to 2 GeV) across the kinematic points, the central nucleon momentum of interest is seen to vary from 2.65 GeV/c to 10.5 GeV/c. Individual calibrations with 'tagged' protons and 'tagged' neutrons will be carried out at the three lowest-Q^2 kinematic points to ensure that the neutron and proton detection efficiencies are well known. As will be seen below, the efficiencies are large and stable for higher Q^2.

4 Apparatus

The use of the ratio method depends upon detection of both scattered neutrons and protons. Potential sources of systematic error arise in determining the acceptance and detection efficiency of these particles. Errors associated with nucleon acceptance can be reduced by matching the neutron and proton acceptances so they cancel in the ratio (as does the electron acceptance and efficiency).

We propose to use the existing BigBite spectrometer in Hall A to measure the momentum and angle of the scattered electrons and the BigHAND detector to detect both the scattered neutrons and protons. Nucleons scattered toward the BigHAND detector will pass through the field of a

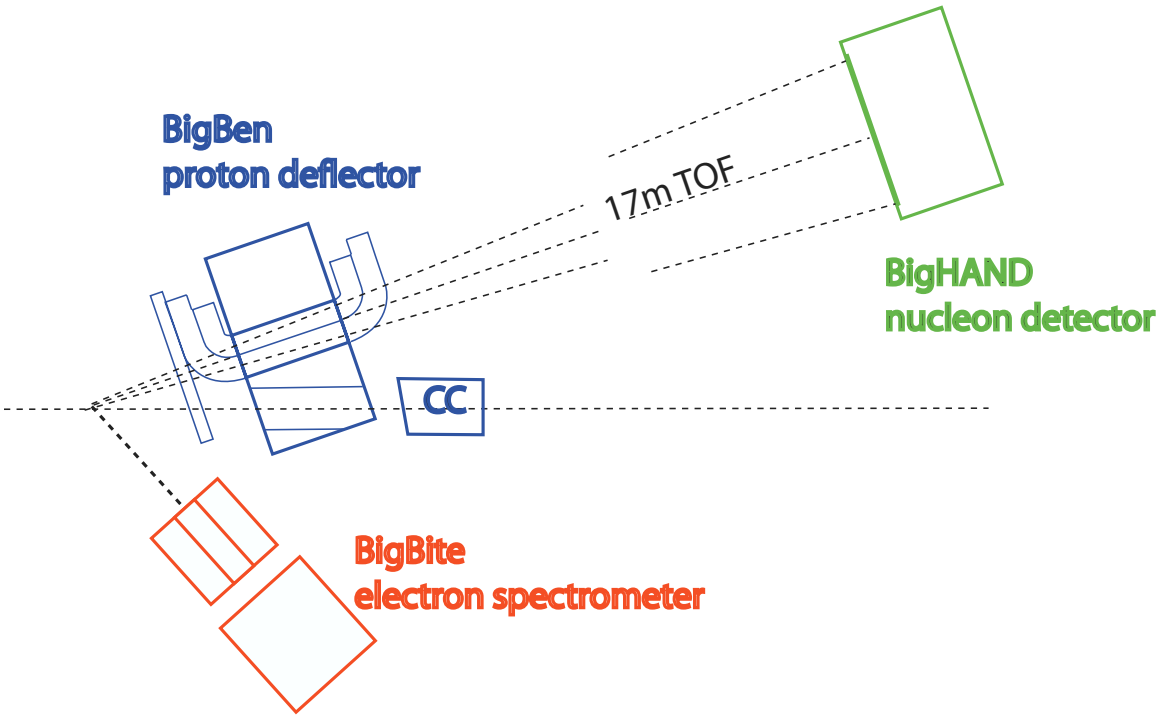

Figure 3: A schematic view of one possible configuration of the apparatus is shown. BigBite will detect scattered electrons while BigHAND will detect the scattered nucleons. The dipole magnet "BigBen" will deflect protons for the purpose of particle identification. The coil configuration shown is one option for avoiding interference between the coils and the beamline. A magnetically-shielded hole in the return iron will allow the unscattered beam to continue on to the beam dump. The corrector coils "CC" will compensate for any effect of residual magnetic field on the beamline. Note: the 17 m flight path to BigHAND is not drawn to scale.

large aperture dipole magnet which will be positioned along the nucleon flight path to vertically deflect protons relative to neutrons. The layout of the experiment is shown schematically in Fig. 3.

The targets will be 10 cm long liquid deuterium (and liquid hydrogen for calibration) cells with 100 μm aluminum windows. This gives about 1.7 g/cm^2 of target compared to about 0.054 g/cm^2 in the windows. As discussed below, selection cuts will reduce the contribution of quasi-elastic events from aluminum below this 3.2% ratio. To obtain percent-level precision, however, it will be necessary to subtract the contribution from the windows. A dummy target cell will be used, having windows at the same position as the real cell but with windows thick enough to give the same luminosity as for a full cell. Sufficient statistics for subtraction of the windows will be obtained by running on the dummy cell for about four percent of the beam time used for the full target.

As discussed below, past experience suggests the BigBite and BigHAND detector rates will be reasonable at a luminosity of 6.7×10^{37}/A /cm^2/s where A is the number of nucleons in the target. For a luminosity of 3.3 $\times 10^{37}$ on a 10 cm deuterium target, the beam current would be 10.5 μA.

BigBite, shown in Fig. 4, is a large acceptance non-focusing magnetic spectrometer. It has a large acceptance (roughly 53 msr in the intended configuration) and has been used successfully at high luminosity ($\approx 10^{37}$/cm^2/s). It will be configured for high momentum measurements, with the

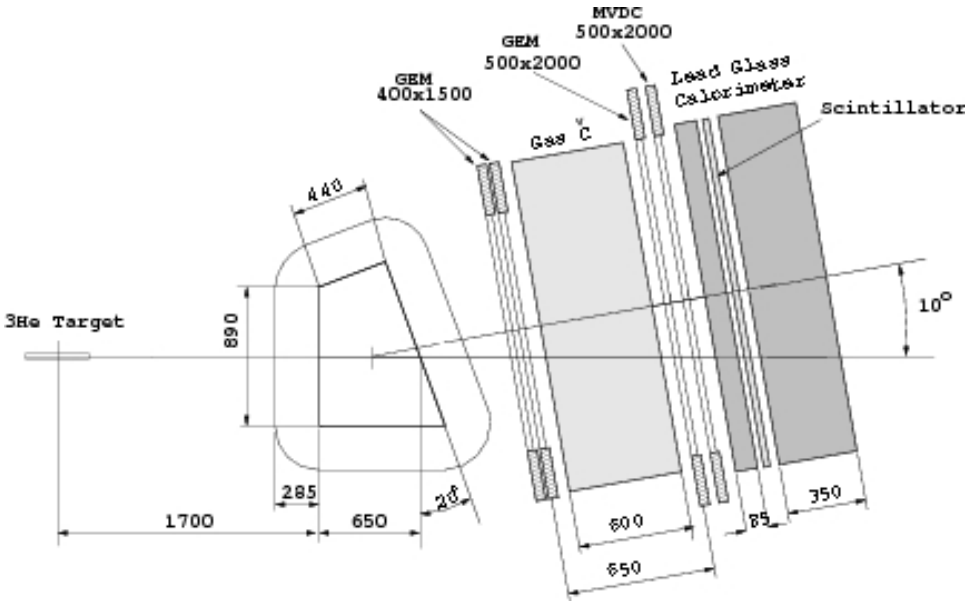

Figure 4: The BigBite spectrometer, configured for high momentum, high luminosity running. Tracking is performed with GEM detectors and a gas Cerenkov counter is located between the detector packages. (The target label refers to another experiment.)

entrance aperture of the dipole 1.55 m from the target and widely spaced coordinate-measuring detector planes For the high luminosity of the experiment, the spectrometer will be instrumented with GEM detector planes. These detectors are planned for use in the polarimeter of the new Super BigBite Spectrometer (SBS) and so will be available for use as the tracking detectors for BigBite. The GEM detectors are designed in a modular form specifically chosen to allow them to be configured to instrument BigBite as well as the new SBS spectrometer. Figure 5 shows how the modules will be assembled to form four tracking planes for BigBite. In this configuration, the expected momentum resolution will be $\sigma_p/p \approx .5\%$ because of the high resolution and small multiple-scattering resulting from the relatively thin GEM detectors. The angular resolution is expected to be better than 1 mr in both horizontal and vertical angles [45].

We intend to run with a single-arm trigger based only upon the electron spectrometer. This eliminates any neutron/proton bias from the trigger and ensures that the trigger efficiency cancels completely in the ratio of interest, R. The lead-glass electromagnetic calorimeter will be used for the trigger of the experiment. As will be discussed in section 10, this is expected to allow a modest single-arm trigger rate of less than 1 kHz. If the gas Cerenkov has been successfully commissioned, it may also be used for redundant rejection of pions in BigBite.

The BigHAND (Hall A Nucleon Detector), shown in Fig. 6, is a large array of scintillators interspersed with seven half-inch thick iron converters which initiate hadronic showers. A "veto" layer on the front face was intended to distinguish neutrons from protons. (An alternative technique will be employed for this measurement, as will be discussed below.) Heavy shielding (2 inches of lead and 1 inch of iron) reduces the electromagnetic rate in the scintillators.

The observed r.m.s. spatial resolution of reconstructed hadronic showers for the GEn experiment [43] is typically 4.3 cm. vertically and 7 cm. horizontally. The detector will be located 17 meters from the target so the corresponding angular resolution will be 2.5 mr and 4 mr (0.15° and .24°),

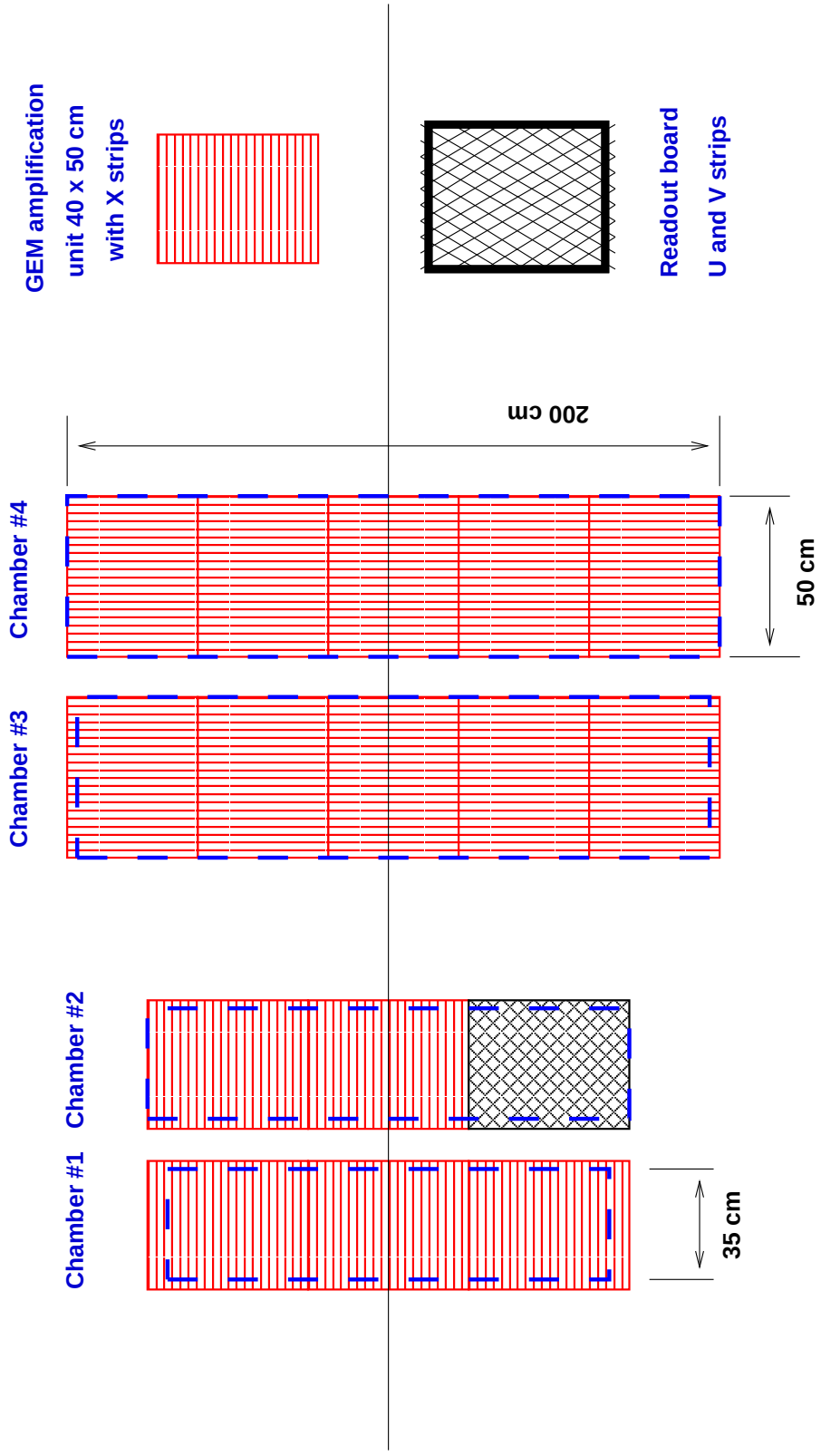

Figure 5: The layout of a 40 cm X 50 cm GEM module is shown along with the arrangements in which the modules would be used to form the four tracking layers for BigBite. The required active area for each layer is shown as a blue dashed line. One Amplification Unit is removed in the diagram to show the U-V readout board.

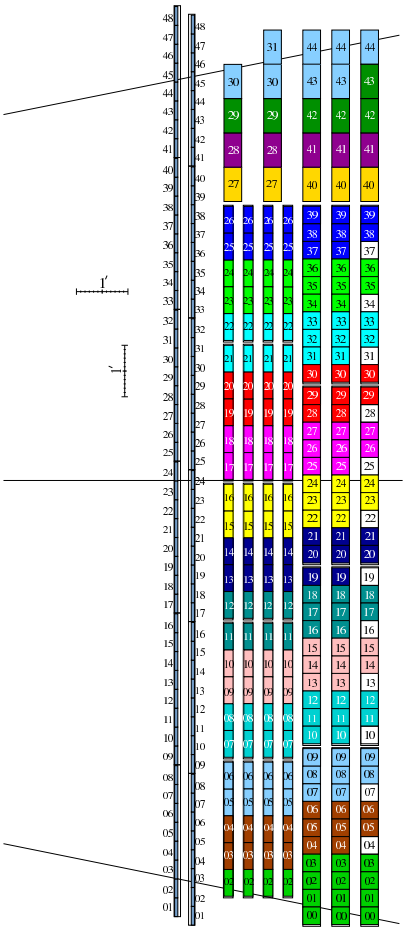

Figure 6: The BigHAND (Hall A Nucleon Detector). Iron converters initiate hadronic showers which are detected by the large scintillators.

respectively. With the higher nucleon momentum of the present proposal, the resolution may be be somewhat improved, especially in the horizontal direction. This excellent resolution will permit critical cuts on the direction of the recoil nucleon relative to the $\vec{q}$-vector direction.

The r.m.s. time-of-flight resolution of the overall detector array is approximately 400 ps [46]. Since the momenta of the nucleons of interest are sharply defined, this will allow tight timing cuts to reject accidentals.With a 17 meter flight path, this will allow clean rejection of low energy nucleons from break-up of nuclei.

The efficiency predicted by simulation [47] for conversion and detection of neutrons and protons in the momentum range of interest is shown in Fig. 7 for a 20 MeV (electron equivalent) threshold. For neutrons, the predicted efficiency is seen to be over 70% at the lowest Q^2 of interest and to rise to over 90% at the highest Q^2. The proton efficiencies are even higher.

As described in the next section, a magnetic 'kick' will be used to distinguish protons from neutrons. We have identified a large-aperture magnet at Brookhaven National Laboratory which could be used for this purpose. This same dipole will serve as the spectrometer magnet for the

Super BigBite spectrometer. In its present configuration, this "48D48" magnet, shown in Fig. 8 has a 120 cm × 120 cm (48 in. × 48 in.) pole face with a 47 cm gap.

The magnet will be modified so it can be positioned near the beam line. This will involve machining a hole through the return yoke to provide a low-field, iron-free region for passage of the outgoing beam. Asymmetric field coils will be needed to avoid interfering with the outgoing beam, One possible solution, shown in Fig. 3, involves the use of an existing standard-coil/booster-coil pair originally designed to drive half of a 100 cm gap magnet. Correcting coils would be used to compensate for beam steering due to any residual fields.

The details of the yoke hole, field coils, field clamps, and correcting coils will be finalized using a magnetic field simulation program such as TOSCA. The magnet modifications will be designed such that the magnet can also be used for the recently-approved high-Q^2 proton elastic cross section experiment [50].

5 Neutron/Proton Identification

If neutron/proton identification were based solely upon the response of the 'veto' layer, then contamination by mis-identification would be a significant problem. Experience from the GEn experiment [43] indicates that about 2.5% of (independently identified) protons fail to fire the veto layer and would be mis-identified as neutrons [44]. More troublesome is the fact that a significant fraction ($\approx 40\%$) of the detected neutrons actually fire the veto layer (because the hadronic shower is initiated in the front shielding). Event topology could be used to more cleanly identify a subset of more unambiguous neutrons or protons but at the cost of a large reduction in detection efficiency.

A much more clean separation of neutrons from protons can be made, without loss of efficiency, by introducing a dipole magnet to deflect the protons vertically. If the initial direction of the nucleon could be accurately predicted, then only a small deflection would be needed to distinguish charged particles from neutral ones. In the case of quasi-elastic scattering, the measured $\vec{q}$-vector does not precisely predict the direction of the struck nucleon's final momentum since the initial momentum of the nucleon within the deuteron also contributes. Using a reasonable model of the deuteron's wave-function [49], the momentum distribution can be determined. It is found that, with 95% probability, the component of the nucleon's momentum along any chosen direction is less than 100 MeV/c. A magnetic 'kick' of 200 MeV/c, then would separate quasi-elastic protons from neutrons at the 95% level. In the simplest analysis, a horizontal line could be defined across the face of BigHAND (for any given event detected in BigBite) such that the struck nucleon would have a 95% probability of falling below the line if the particle were a neutron and a 95% probability of falling above the line if the particle were a proton.

The remaining 5% mis-identification can still be accurately corrected by using the 'veto' layer (and possibly event topology) to determine the actual distribution of neutron and proton events relative to the ideal positions they would have for elastic kinematics. In particular the spread of the neutron distribution relative to the $\vec{q}$-vector can be investigated by studying the sample which do not fire the veto (and making a modest correction for protons). Also, since the initial momenta of the nucleons are vertically symmetric, the actual distributions of neutron and proton events can be empirically determined by observing the distributions of those neutrons which are displaced downward from the point predicted for elastic kinematics and those protons which are displaced upwards from the (magnetically deflected) point predicted for elastic kinematics. Either of these

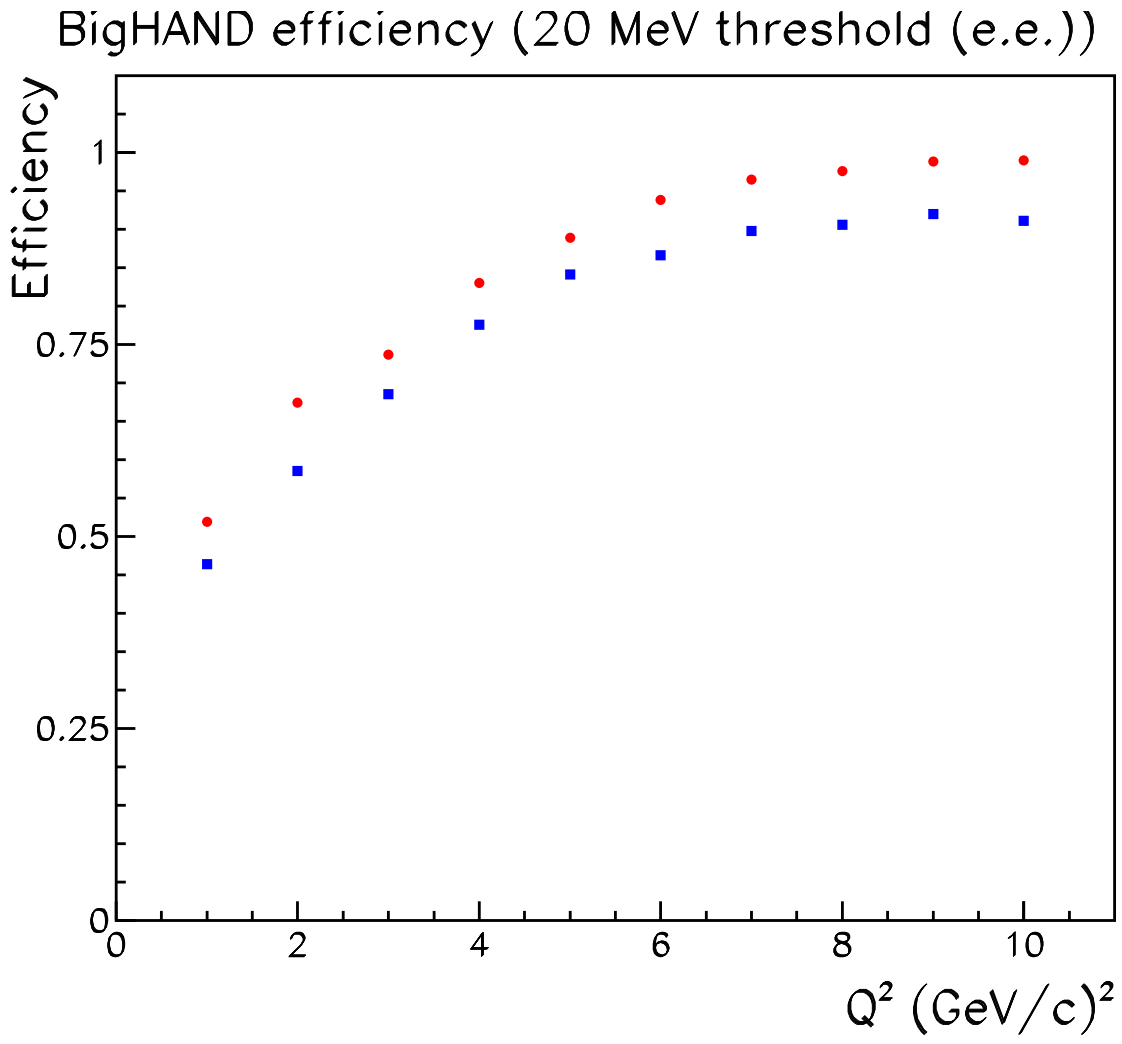

Figure 7: The predicted [47] detection efficiency of BigHAND is shown for neutrons (blue squares) and protons (red circles) as a function of the central nucleon momentum associated with each Q^2.

Table 2: Field strength for deflection dipole is given for each of the proposed kinematics. Also given are $\Delta_{\rm pn}$, the separation on BigHAND between an undeflected neutron and a deflected proton having the same $\vec{q}$-vector, and $P_{\rm kick}$, the effective vertical momentum 'kick' given by the dipole.

Q^2 (GeV/c)^2	3.5	4.5	6.0	8.5	10.	12.	13.5	16.	18.
$\int Bdl$ (T-m)	0.85	0.85	0.85	0.91	1.05	1.24	1.37	1.60	1.88
$\Delta_{\rm pn}$(cm)	129	107	85	68	68	68	68	68	68
p_{kick}(MeV/c)	200	200	200	214	247	292	322	376	442

correction techniques should allow the systematic errors due to neutron/proton mis-identification to be reduced to well below 1%, and the comparison of the two techniques should allow the confident determination of this contribution to systematic error.

The 200 MeV/c kick required to separate quasi-elastic protons from neutrons can be achieved by applying a dipole field, near the beginning of the flight path, having a field integral of $\int Bdl \approx 0.85$ T·m.

For high Q^2, a 200 MeV/c kick would give a relatively small spatial separation on the BigHAND detectors. A proportionally larger field will be used to ensure an adequate displacement. Table 2 gives the field integrals assumed in the Monte Carlo simulations presented below. Also given are the resulting mean separations between the undeflected neutrons and the deflected protons. For low Q^2 a larger deflection not be an advantage as it would deflect protons out of BigHAND acceptance so they would be lost. (See the discussion of fiducial cuts below.)

An alternate technique may be employed, at low Q^2, to use the deflection magnet to achieve neutron/proton identification. This involves making two sets of measurements, one with the field on and and one with the field off. The field-on measurements would be used only to measure neutron-coincident events, indicated by the proximity of the BigHAND hit to the position expected based on the $\vec{q}$-direction. The field-off measurement would be used to measure the sum of the neutron-coincident and proton-coincident events. The number of proton coincidences would then be determined as the difference between these measurements. There are two advantages of this technique over the simultaneous measurements described above. The BigHAND acceptance is guaranteed to be identical for both types of event since they are both detected in the same region of BigHAND, with no deflection. Also there is no loss in acceptance resulting from the use of a strong dipole field so the separation can be improved by using as strong a field as practical. The apparent disadvantages of the technique are that more beam time is needed to make the two separate measurements and that there is a loss in statistical accuracy for the proton-tagged events due to error propagation. Both of these disadvantages are negligible for the very high coincidence rates which will occur for the low-Q^2 points. The choice between these techniques for low-Q^2 measurements will be based on further simulation. For the higher-Q^2 points, simultaneous measurements present a clear advantage in rates. For the purpose of the discussion and simulations presented in section 9 here, simultaneous measurement of proton-coincident and neutron-coincident events have been assumed.

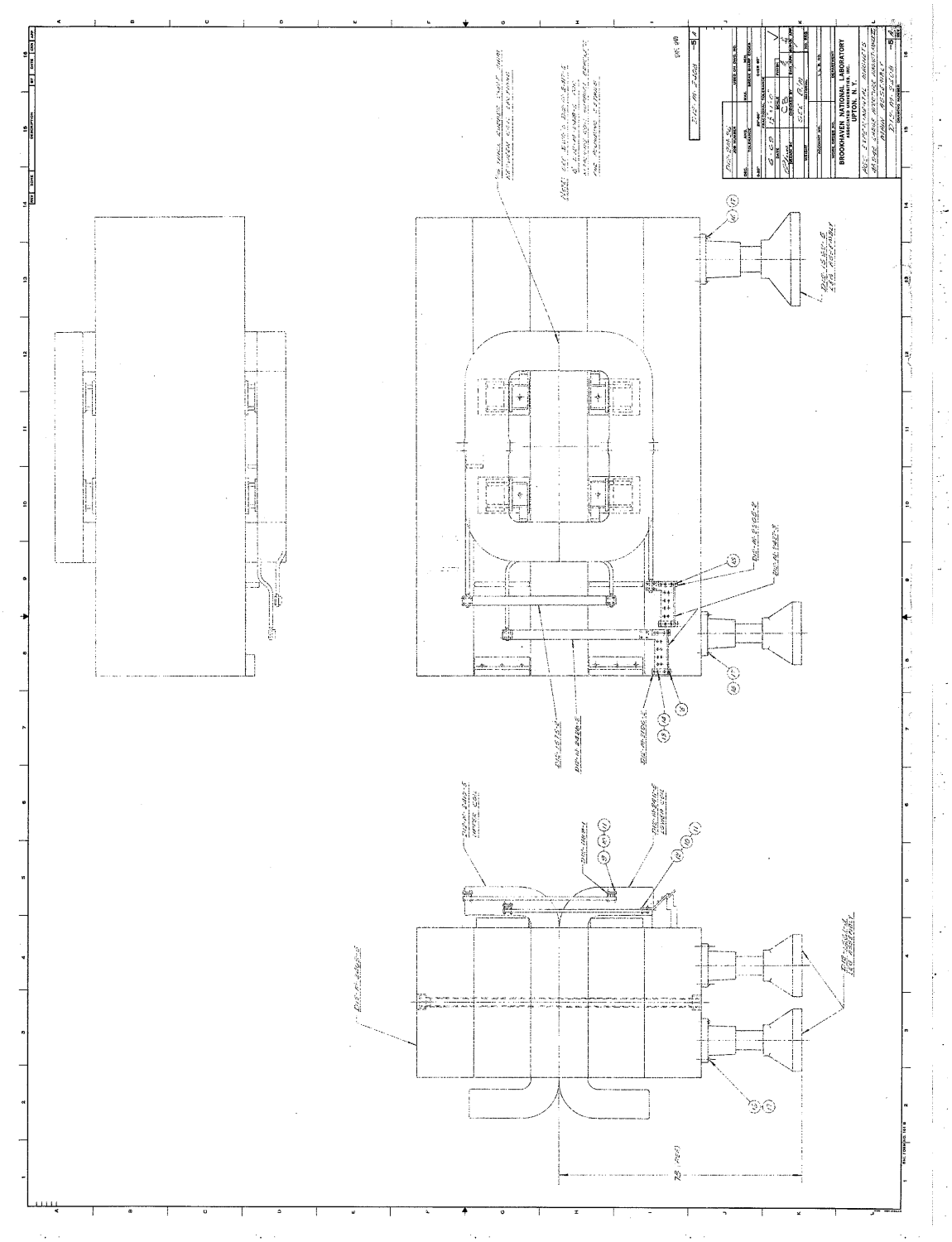

Figure 8: Assembly diagram for generic 48D48 spectrometer magnet. Magnet is shown mounted for horizontal bend-plane but will be used for vertical bend plane. Coil configuration shown is that used at BNL.

6 Acceptance and Fiducial Cuts

Here we discuss event-selection cuts which will be applied to ensure that the systematic errors due to acceptance losses remain very small.

In the case of elastic kinematics (applicable for the calibration reactions discussed in the next section) there is a direct mapping of scattered-electron direction to recoiling-nucleon direction. The acceptance of both BigBite and BigHAND can be conveniently expressed in terms of the electron-scattering angles. The solid angle for acceptance of coincidence events is then found from the overlap of the acceptance of the two detector systems. This is shown, for the nine kinematic points, in Fig. 9 with the full geometric acceptance of BigBite and a reduced acceptance of BigHAND, as discussed below. At the lowest-Q^2 points, BigHAND is a limiting aperture and fiducial cuts will be needed to restrict events for which the nucleon misses it. At large Q^2 the acceptance is limited by BigBite and the coincident events fall in a small region at the center of BigHAND.

For quasi-elastic events, the $\vec{q}$-vector can be reconstructed based on the scattered-electron momentum and direction measured by BigBite. A fiducial cut can be placed on the direction of $\vec{q}$ to choose the central direction of the scattered nucleons. While Fermi motion will widen the image, the ideal case of elastic scattering can be used to map the acceptance to a position distribution of neutrons on BigHAND (and a similar proton distribution, taking into account the deflection by the dipole magnet). The green overlap regions in Fig. 9 represent the angular region of the BigBite acceptance for which scattering at elastic kinematics would send a nucleon into the BigHAND acceptance regardless whether it was a neutron or proton. Potential systematic errors are greatly reduced by *using the same fiducial region for both neutron-coincident and proton-coincident measurements*. The 'image' of the fiducial region projected onto BigHAND will differ for protons and neutrons because of the vertical kick given to the protons by the dipole magnet. To first order, the effect of this offset can be prevented from introducing a difference in acceptance by using a reduced fiducial region. To determine whether a particular (θ, ϕ) point is within the fiducial, the direction and magnitude of the corresponding $\vec{q}$ for elastic scattering are determined. The trajectories are evaluated for both a neutron and a proton with that momentum. Only if both such particles would fall in the active region of BigHAND is the angular point within the fiducial.

As a result of the fiducial cut, the neutron image for the accepted elastic events would leave an empty strip at the top of the BigHAND acceptance. The size of this strip is determined by the shift in the proton image relative to the neutron image. Similarly the elastic protons occupy the top of BigHAND acceptance, leaving an unoccupied strip at the bottom of acceptance. The size of the strip follows from the vertical kick given to the protons by the dipole, the nucleon momentum, p_N, and the distance, L from the target to BigHAND. While quasi-elastic protons (and neutrons) are not guaranteed to remain within the acceptance, the matching of the acceptance losses is improved by this reduced fiducial cut. Reducing the size of BigHAND by this strip of size $D = \frac{\Delta p}{p_N} L$ at the top when calculating the elastic neutron acceptance gives the BigHAND coverage shown in Fig. 9.

A further refinement will be used for the two lowest-Q^2 kinematic points, to reduce systematics. For the Q^2=3.5 and 4.5 (GeV/c)^2 points, the combined elastic acceptance would be largely determined by BigHAND if the full BigBite acceptance shown in Fig. 9 were used. So elastic events selected by such a fiducial would have scattered nucleons extending to the edge of the BigHAND acceptance. With the addition of Fermi motion, the quasi-elastic events may be expected to have a larger loss, by falling outside the BigHAND acceptance, than would be the case at the other kinematic points. Monte Carlo simulation (described in section 8.1) confirms that the accep-

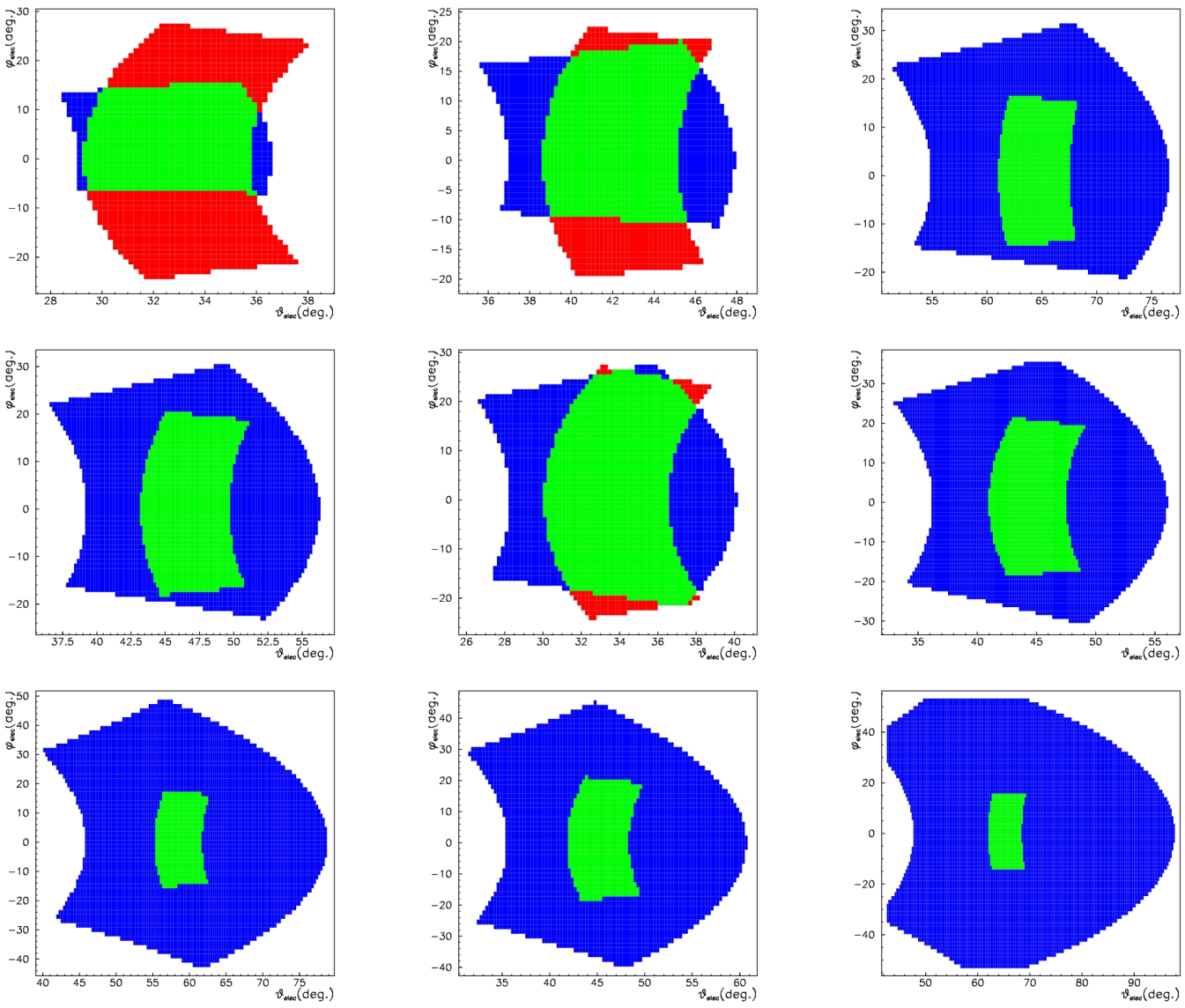

Figure 9: The acceptance of BigBite as a function of electron scattering angles (θ, ϕ) is shown in red, the acceptance of BigHAND for elastically scattered neutrons *as a function of the electron scattering angles* is shown in blue. Overlap (corresponding to coincident acceptance for elastic events) is shown in green. The acceptance of BigHAND used for the plot is a subset for which an elastic proton would also fall in the active area. The plots correspond to the kinematics of the experiment (see Table 1). From left to right, the plots represent: Upper row, $Q^2 = 3.5$, 4.5, 6.0; Middle row, $Q^2 = 8.5$, 10., 12.; lower row, $Q^2 = 13.5$, 16., 18. $(\mathrm{GeV/c})^2$.

tance losses are larger at these kinematics, amounting to 14.4% and 9.4% for the lower and higher Q^2, respectively. To the extent that these acceptance losses are equal for protons and neutrons, they cancel in the ratio R'' (Eqn. 1). Systematic errors may arise, however, due to difference in the acceptance-corrections resulting from effects such as horizontal steering by the dipole's field, multiple-scattering, or edge effects in nucleon detection efficiency. It is therefore prudent to reduce the acceptance corrections where practical. This can be effected by choosing a new smaller fiducial, based on BigBite measurements, by demanding that the $\vec{q}$ vector point towards a further-reduced portion of the BigHAND face. A margin of safety, d, is excluded around all edges. This defines a smaller 'active' area of BigHAND to be used in defining the fiducial cut. If d is chosen as $d = \frac{\delta}{p_N} L$ then, to first order, quasi-elastic coincidences with the electron within the fiducial cut will be lost only if the struck nucleon had a component of momentum of at least δ directed towards the edge of BigHAND. In addition, to match neutron and proton acceptances, events are rejected if *either* a neutron or a proton with the corresponding $\vec{q}$ would pass near the top or bottom of BigHAND, within a distance corresponding to $\delta = 100$ MeV/c. The cost of applying this tighter fiducial cut is a smaller fractional acceptance for quasi-elastically scattered electrons. The rate calculations in this proposal are based upon fiducial cuts corresponding to $\delta = 80$ MeV/c for Q^2 =3.5 (GeV/c)^2 and $\delta = 40$ MeV/c for the Q^2 =4.5. With these cuts, the estimated loss of acceptance due to Fermi motion will be less than 5% at all kinematic points. This limits the potential for systematic errors due to the difference in the loss of protons compared to neutrons. The cost of these cuts is a reduction by 60% in the counting rate at the lowest Q^2 point and by 17% at Q^2 =4.5 (GeV/c)^2. Since the count rates are very high at these kinematic points, the loss of acceptance is justified by the decreased sensitivity to systematic error.

7 Nucleon Detection Efficiency Calibration

While the efficiency of electron-detection cancels in the ratio, R''(equation 1), that is not true for the neutron or proton detection efficiencies. The efficiency of BigHAND's detection of these particles could be calculated in Monte Carlo, as has been done for lower energies [47], but a reliable determination of the efficiency at the percent level will require calibration with tagged sources of known protons and neutrons over part of the kinematic range. As shown in Fig. 7, the efficiency is large and quite constant for $Q^2 > 8$ (GeV/c)^2. Below that, however it changes rapidly as a function of nucleon momentum. In that region, the calculation of efficiency is likely to be more sensitive to the details of the detector description. It is important to have reliable efficiency calibrations there.

Fortunately the efficiency may be expected to be quite stable since it is largely determined by the mass distribution in the detector and the resulting probability of hadronic shower initiation. Factors, such as gain, threshold, and light yield have a relatively minor effect since most showers produce large numbers of secondaries and so their total light output is well above threshold. This stability is demonstrated in Fig. 10 which shows the *ratio* of the efficiency found [47] for a threshold of 20 MeV (electron equivalent) to that found with a threshold of only 5 MeV (electron equivalent). Even at the lowest Q^2 of interest, 3.5 (GeV/c)^2, such a huge change in threshold would result in only $\approx 10\%$ change in efficiency. This is in contrast to detection of low energy neutrons in scintillator, for which the detection efficiency is a strong function of effective threshold. Furthermore, since BigHAND's detection is based purely on scintillation, it is immune to the rapid changes in efficiency and background which can more typically occur in wire chambers. Because the efficiency will be

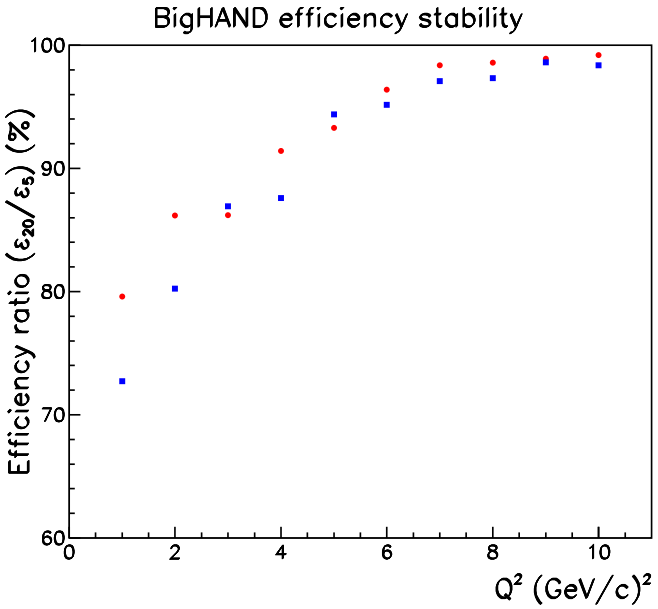

Figure 10: The predicted [47] *ratio* of the detection efficiency of BigHAND with a threshold of 20 MeV(ee) compared to a threshold of 5 MeV(ee) is shown for neutrons (blue squares) and protons (red circles) as a function of the central nucleon momentum associated with each Q^2. (Displacement of individual points from the overall curve is due to finite Monte Carlo statistics in the simulation.)

stable, it is sufficient to have separate calibration runs, rather than simultaneously taking calibration data by having the calibration target in place along with the deuterium target.

Efficiency measurements, as described below, are planned for the three lowest kinematic settings, $Q^2 = 3.5$, 4.5 and 6.0 $(GeV/c)^2$. In addition, the analysis of this data may benefit from calibration measurements planned as part of the proposed GEN experiment [40] which plans to make similar efficiency measurements at $Q^2 = 5$, 7 and 9.5 $(GeV/c)^2$.

For both protons and neutrons, the basis of the calibrations is a cleanly identified reaction on the proton which produces a 'tagged' nucleon with a known momentum vector, (p(e,e′)p for proton calibration and p(γ,π^+)n for neutron calibration). BigHAND is then searched for the nucleon near the expected position and the detection efficiency is determined as the ratio of the number of tagged events for which the nucleon is found to the total number of tagged events.

7.1 BigHAND Calibration Coverage

The $p(e, e'p)$ proton-calibration reaction and the $p(\gamma, \pi^+ n)$ neutron calibration reaction have essentially the same (elastic-scattering) kinematics. A disadvantage of the use of elastic kinematics for calibration is that the acceptance of BigBite for electrons maps into a well-defined corresponding angular range on the BigHAND detector face (see Fig. 11). Regions beyond that, which would not be illuminated by calibration particles, may still be of interest for quasi-elastic events since the particles are then smeared beyond the strict elastic kinematic boundaries by the nucleon's initial momentum. To reduce the impact of the larger 'footprint' of quasi-elastic events, calibration data will be taken at two positions of the BigBite spectrometer so the face of BigHAND will be more

Table 3: Fraction of detected quasi-elastic nucleons which fall inside the region calibrated (at the same kinematic point) with a) a single BigBite position for calibration or b) two off-set calibration positions.

Q^2 (GeV/c)^2	a) Fraction (%) in Single Cal. Zone	b) Fraction (%) in Double Cal. Zone
3.5	97.7	100.
4.5	82.3	99.7
6.0	56.9	83.4

widely illuminated by calibration nucleons. This expanded calibration region is illustrated in Fig. 12 which also shows the distribution of quasi-elastic nucleons coincident with electrons within the fiducial region selected by BigBite. (The simulation is described in section 8.1.) Table 3 shows the predicted fraction of quasi-elastic coincidence events for which the detected nucleon will fall inside this calibration region. While the use of two calibration positions is not required at the Q^2=3.5 (GeV/c)^2 point, it affords an excellent opportunity to illuminate the entire BigHAND face with calibration events. For the Q^2=6.0 (GeV/c)^2 point, further improvement could be made in the fraction of quasielastic events within the calibrated region by using three BigBite positions (91.5% calibrated) or even four BigBite positions (93.1% calibrated) but the results obtained with two positions (83.4% calibrated) are sufficient. The extrapolation of the calibration at this setting will be included in the systematic error analysis. As described below, extrapolation of lower-momentum calibration data will also be used to estimate efficiencies for those events which are outside the elastic-calibration region at the momentum of interest.

Calibration measurements will be made only at the three kinematic points shown in Fig. 12 and listed in Table 3. The systematic errors due to the extrapolation of the nucleon detection efficiencies can be conservatively estimated to be under 2%. The hadronic cross sections change quite slowly in the region in which these interpolations will be made (above the nucleon momenta indicated by arrows in Fig.13), as a result of which the estimated efficiencies shown in Fig. 7 change only moderately in the regions of interest. The method of interpolation is described in the next paragraph.

Those regions of BigHAND which are not directly calibrated at a particular nucleon momentum will be illuminated by the lower momentum calibration nucleons at other kinematic points. In this case Monte Carlo simulation, tuned using the lower energy measurements, will be used to extrapolate the efficiency calibration to the momentum of interest. Essentially, the observed efficiency at lower momentum can be used to determine an effective number of interaction lengths in sub-regions of the detector. The effective thickness can then be scaled to higher momentum by taking into account the known variation of hadronic cross-sections with momentum and a new efficiency can be predicted. This is a modest extrapolation since the hadronic cross sections change slowly as the nucleon momentum changes over the range from 2.6 to 10.5 GeV/c (see Fig. 13). This results in the slow variation in BigHAND's efficiency seen in Fig. 7. The efficiency variation is expected to be quite modest over the entire range of interest ($3.5 \leq Q^2 \leq 18.0$ (GeV/c)^2) and to be almost constant at the highest Q^2. Since Fig. 7 shows the efficiency to be changing very slowly in this kinematic range (Fig. 13 shows the nucleon cross-section to be essentially flat for the corresponding

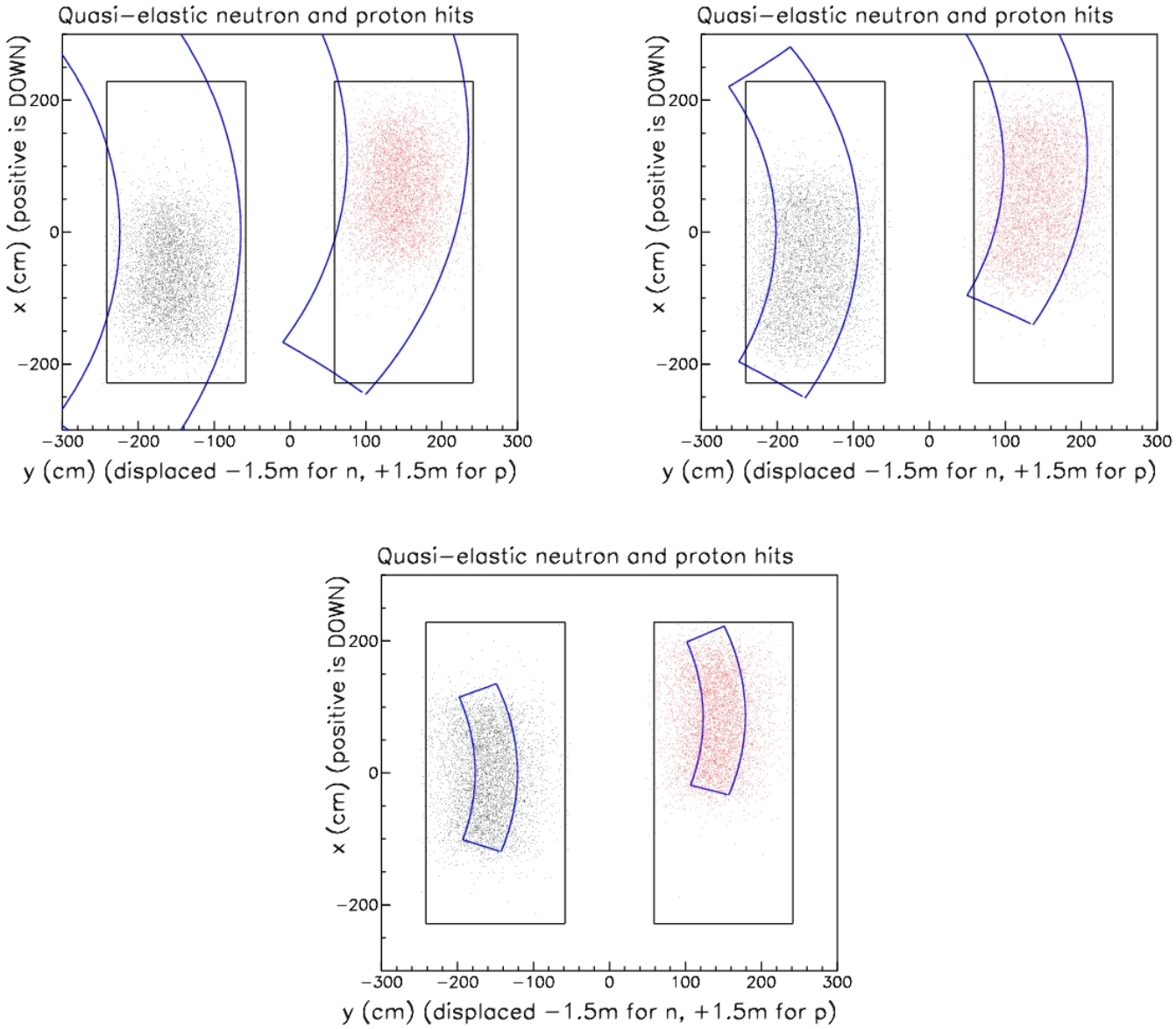

Figure 11: The face of the BigHAND detector is shown (rectangle) with a superimposed blue outline of the region covered by elastically scattered (calibration) nucleons for which the corresponding electron falls within the acceptance of BigBite when BigBite is positioned at the nominal scattering angle. For clarity the image for neutrons and protons are shown side-by-side rather than superimposed. Note that positive-x is downward, so the images are inverted. Dots indicate positions of neutron (black) or proton (red) hits from simulated quasi-elastic events subject to the fiducial cut. The three plots correspond to the kinematic points at which calibration measurements will be made: Top left, $Q^2 = 3.5$; Top right, $Q^2 = 4.5$; Bottom, $Q^2 = 6.0$ (GeV/c)^2.

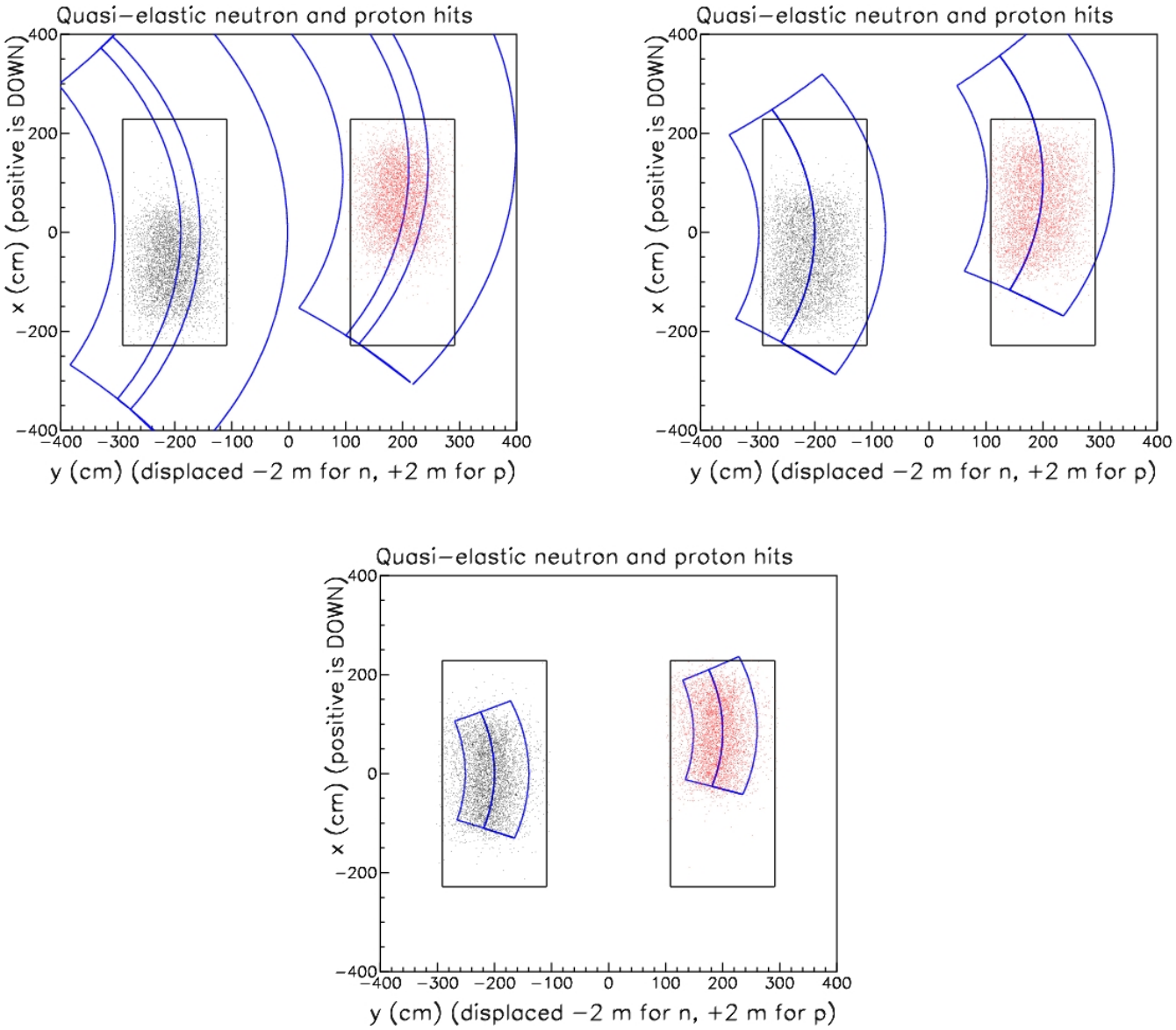

Figure 12: The face of the BigHAND detector is shown (rectangle) with a superimposed blue outline of the region covered by elastically scattered (calibration) nucleons for which the corresponding electron falls within the acceptance of BigBite when BigBite is positioned at two planned calibration angles. For clarity the images for neutrons and for protons are shown side-by-side rather than superimposed. Note that positive-x is downward, so the images are inverted. Dots indicate positions of neutron (black) or proton (red) hits from simulated quasi-elastic events subject to the fiducial cut. The three plots correspond to the kinematic points at which calibration measurements will be made: Top left, $Q^2 = 3.5$; Top right, $Q^2 = 4.5$; Bottom, $Q^2 = 6.0$ (GeV/c)^2.

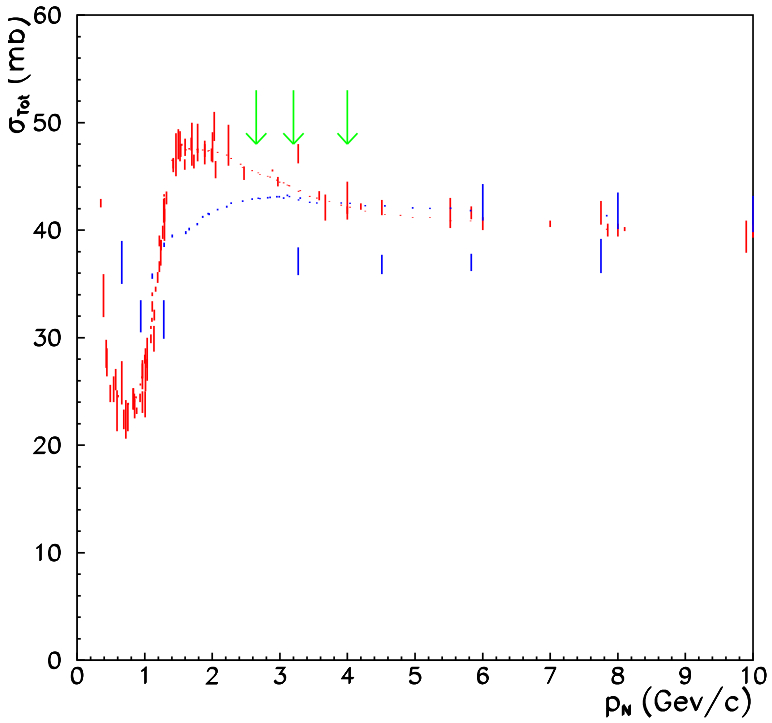

Figure 13: Total cross section [51] for proton-proton (red) and proton-neutron(blue). Some points with large errors have been suppressed. Green arrows indicate the central nucleon momenta for the three kinematic points at which calibration data will be taken.

momentum (p_N >4.3 GeV/c).), this extrapolation is expected to have small uncertainty. Despite the large size of BigHAND, a portion (one tenth) of its structure could be brought to the tagged neutron beam at Dubna for calibration. This could provide a cross check of the Monte Carlo simulation of momentum-dependence of efficiency at high nucleon momentum.

7.2 Proton Calibration

Calibration of the detection efficiency for protons can be done straightforwardly, using a hydrogen target in place of the deuterium target and using BigBite to select elastic-scattering events. The recoil elastic protons have the same momentum as the protons at the center of the quasi-elastic peak, and so are ideal for calibrating the efficiency.

Clean selection of tagged protons requires that BigBite be able to distinguish elastic events with negligible contamination from inelastic events, for which the 'tagged' nucleon might be absent or at a significantly different angle than predicted. Figure 14 shows the kinematic locus for elastic scattering kinematics (in the region of each of the highest-Q^2 kinematic point for which calibration measurements are planned) and the locus of the scattered-electron kinematics for pion-production threshold. The two are seen to be cleanly separated in both angle and energy. The bars superimposed on the plots indicate the anticipated resolution of BigBite in angle and energy.

As discussed above, the coverage of the calibration will be extended across a wider region of

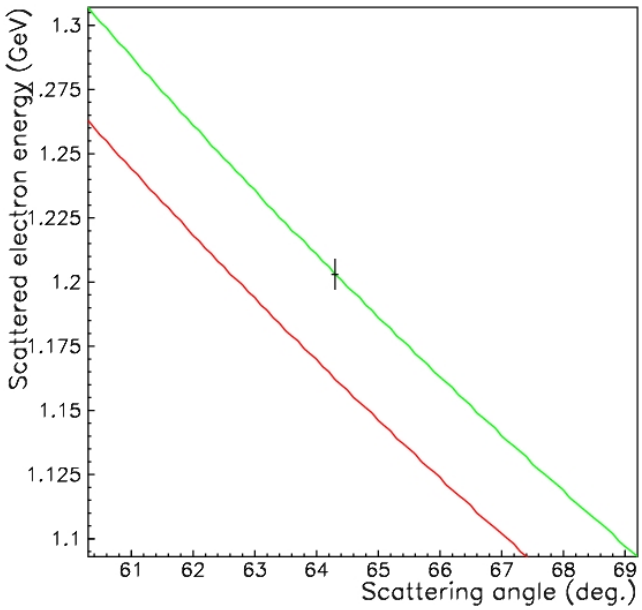

Figure 14: Scattered electron energy versus angle for elastic scattering from the nucleon (green) and for pion-production threshold (red). The bars indicate the BigBite resolution in momentum and angle. The plot shows the clean kinematic separation at the $Q^2 = 6.0$ (GeV/c)^2 kinematic point. The separation is even cleaner at the other kinematics for which calibration measurements are planned.

BigHAND by taking calibration data in two BigBite positions, as represented in Fig. 12.

7.3 Neutron Calibration

A clean *in situ* source of tagged neutrons at essentially elastic-scattering kinematics can be generated using a radiator to produce real photons which, in turn, produce neutrons through the p(γ, π^+)n reaction on a Hydrogen target. The calibration for each kinematic setting will be done at the same two BigBite settings discussed above for proton efficiency calibration. Since the kinematics of the reaction are essentially those of elastic scattering, the overlap of the calibration neutron spectrum with the quasielastic spectrum is the same.

The end-point method can be used to select the reaction of interest and exclude multi-body final states. In particular, for each beam energy, the maximum possible π^+ momentum for three-body p$(\gamma, \pi^+)\pi$N reaction sets the scale of the lowest π^+ momentum which can safely be used to select the desired two-body channel. Clear identification of the exclusive p(γ, π^+)n reaction will be ensured by requiring that the π^+ momentum be at least 1.5% above the kinematic limit for the three-body channel. With 0.5% momentum resolution in BigBite, the 1.5% gap between the lowest π^+ momentum used and the highest momentum from 2π-production provides an adequate safety margin. Production of 2π background at this kinematic limit will be negligible both because it requires photons at the bremsstrahlung end point and because the phase-space vanishes. This minimum acceptable π^+ momentum, in turn sets the limit for the minimum usable photon energy

Table 4: Kinematics limiting the part of bremsstrahlung spectrum which can be used for neutron efficiency calibration.

Q^2 $(GeV/c)^2$	E_{beam} (GeV)	θ_e	E_π^{max} (γ,π) (GeV)	E_π^{max} $(\gamma,2\pi)$ (GeV)	E_π^{limit} (γ,π) (GeV)	E_γ^{min} (GeV)	$\int\ \Gamma\ dk$
3.5	4.4	32.5°	2.54	2.453	2.494	4.25	0.0023
4.5	4.4	41.9°	2.00	1.928	1.96	4.21	0.0030
6.0	4.4	64.3°	1.20	1.16	1.18	4.12	0.0046

For each kinematic point, the values given are: $E_\pi^{max}(\gamma,\pi)$, the end-point energy for π production; $E_\pi^{max}(\gamma,2\pi)$, the π end-point energy for 2π production; $E_\pi^{limit}(\gamma,\pi)$, the minimum π energy to be used for calibration (to exclude $E_\pi^{max}(\gamma,2\pi)$ by 1.5%); E_γ^{min}, minimum photon energy giving $E_\pi(\gamma,\pi)$ above $E_\pi^{limit}(\gamma,\pi)$; $\int\ \Gamma\ dk$, the photon flux (per electron) integrated [48] from E_γ^{min} to the photon end point (assuming 6% Cu radiator).

and the part of the bremsstrahlung end-point region which will actually be used for calibration events. Table 4 shows the region of the photon end point which can be used for neutron calibration at each kinematic setting. For the lowest Q^2 point, for example, the three-body reaction cannot produce pions above 2.453 GeV. For safety, pions will be identified as coming from the two-body calibration reaction only if they lie between 2.494 GeV and the kinematic limit of 2.54 GeV.

The real photons used for the $p(\gamma,\pi^+)n$ calibration reaction will be generated using a copper 6% radiator upstream of the LH_2 target. Maintaining the same limit on rate in BigBite then requires that the beam current be reduced by a factor of four for these measurements. While real photons interacting with well-defined 2-body kinematics will dominate, roughly one quarter of the rate is expected to originate from virtual-photon interactions. The virtual-photon contribution can be studied (along with the corresponding distribution of neutrons in BigHAND) by running without a radiator and measuring neutrons associated with the $p(e,\pi^+)$ reaction. Because this is a relatively small correction, allocation of beam time would be optimized to yield the minimal error on the real-photon calibration by spending only a fraction as much beam time on running without a radiator. (Taking the virtual and real cross sections to be equal and the neutron acceptance and efficiencies to be as large for virtual production implies that the error bar would be minimized by dedicating 20% of the neutron-calibration time to running without a radiator.)

8 Simulations

At high Q^2 the kinematic separation of quasi-elastic and inelastic events becomes more washed-out by the kinematic-broadening effects of Fermi motion in the deuteron. Also the size of the inelastic cross section relative to the quasi-elastic grows rapidly with increasing Q^2. A simulation is needed to determine whether there is a serious problem with contamination of the quasi-elastic coincidence signal by inelastic events for which a nucleon accidentally hits the BigHAND near where a quasi-elastic nucleon would be expected.

This section will present the technical details of the implementation of the simulations, including the normalization of the inelastic spectrum relative to the quasi-elastic. The next section will present

the results of the simulations.

8.1 Quasi-elastic

Simulation of the quasi-elastic signal was carried out in a spectator model in which the virtual photon was assumed to interact with only one nucleon while the other simply escaped. This implies that the spectator nucleon is projected into 'on-shell' kinematics by the interaction (with whatever initial momentum it has) and so the initial off-shell mass of the struck nucleon is determined by the requirements of energy conservation. While off-shell effects were included at the kinematic level, no attempt was made to modify the electron-nucleon scattering cross section to reflect the off-shell nature of the struck nucleon. For these simple signal-to-noise estimates, the scaled dipole form factors were assumed for the nucleons (except the Galster parameterization was used for the neutron electric form factor). As described below, kinematic effects of the initial motion of the nucleon were reflected by calculating the cross section based on the electron energy and scattering angle as determined in the rest frame of the scattered nucleon.

The momentum distribution of nucleons was taken from the momentum-space wave-function (non-relativistic Fourier transform of spatial wave-function) for a Lomon and Feshbach deuteron potential. The particular model used (#10 from reference [49]) gave 5.79% D-state and included a hard core. The hard core is reflected in a high-momentum tail in the momentum-space wave-function making this a somewhat 'worst case' simulation.

In brief, the steps of each quasi-elastic event simulation are summarized here. A Fermi momentum was chosen for the struck nucleon based on the probability distribution for magnitude of p derived from the deuteron wave-function. A direction was chosen isotropically. The corresponding kinetic energy of the the on-shell spectator was subtracted from the deuteron mass to find the kinematically-consistent initial energy of the struck nucleon from which the (off-shell) invariant mass of the struck nucleon was found. The beam electron was then rotated and boosted to a frame in which the nucleon was at rest (and the electron was rotated back onto the z-axis). A scattering angle was then chosen isotropically (flat in ϕ and in $\cos\theta$) and the elastic scattering cross section was evaluated for these rest-frame initial kinematics. The scattered energy was calculated with the added requirement that the off-shell initial-state nucleon be promoted to an on-shell nucleon in the final state. Some 'sanity cuts' were applied to eliminate extreme cases in which the quasi-elastic model was clearly pushed beyond the range of applicability, such as cases with off-shell invariant mass of the struck nucleon being less than 10% of the nucleon mass or final electron energy being unphysical. All boosts and rotations were then inverted on the final-state particles to return them to the lab frame. No kinematic weighting was done on the distributions of Fermi momentum or scattering angle to reflect the greater probability of scattering at small angles and at kinematics which lead to lower electron energy in the nucleon rest frame. The higher weighting of these events was reflected in the calculated cross section, which was then used to weight the entries made to the final-state distributions. Thus the simulation not only properly accounted for these kinematic effects, it also resulted in properly normalized cross sections for the simulated reaction. To select the quasi-elastic events of interest, an acceptance cut was imposed to require that the electron fell into the BigBite acceptance while the scattered nucleon fell into the BigHAND acceptance. The effects of finite-resolution were then incorporated by smearing the final electron-energy angle and energy by Gaussian distributions to simulate the BigBite resolution and similarly smearing the detected nucleon angle to reflect the BigHAND resolution. The resulting quantities were then used to calculate

W^2 and θ_{pq} and the simulated distributions of the quantities of interest were incremented, weighted by cross section. Here θ_{pq}, introduced above, is the angle between the calculated $\vec{q}$ direction and the observed scattered nucleon direction while W^2 is the squared missing-mass of the hadronic system as calculated assuming a stationary proton target (i.e. $W^2 = (m_p + \omega)^2 - (\vec{q})^2 = m_p^2 + 2m_p\omega - Q^2$).

8.2 Inelastic

The term "inelastic" is used here to imply particle production and is exclusive of quasi-elastic events. Simulation of inelastic events required a more sophisticated model for the basic interaction on the nucleon. This was done with the use of the Genev physics Monte-Carlo [52] written by the Genoa group and used extensively in simulations for CLAS. This program is designed to simulate with, reasonable empirical distributions, production of multi-pion final states and production and decay of Delta's, rho mesons, and omega meson (phi meson production was not enabled when the simulations were run). It can simulate neutron or proton targets and both were used in simulating inelastic events from the deuteron.

The smearing effects of Fermi motion for quasi-free inelastic production from the nucleons in the deuteron were included in a similar way to that described above for the quasi-elastic production. There was, however, no mechanism to put the initial-state nucleon off-shell for the initial state used by Genev. The spectator model was therefore implemented by treating the initial state as two on-shell nucleons with equal and opposite Fermi-momentum (in the deuteron rest frame). The effective violation of conservation of energy implied by this approximation is modest (a few tens of MeV) and is expected to have the effect of widening tails and so causing backgrounds to be over-estimated if anything.

Final-state distributions were simulated separately for electro-production off the neutron and proton. The same momentum-state wave-function was used to generate the initial momentum distribution of the target nucleons. After rotating and boosting to the nucleon rest frame the energy of the incident electron was passed to a Genev-based subroutine which simulated a single inelastic event for the chosen effective beam energy. The scattered electron direction was selected randomly (both θ and azimuthal angle, ϕ) by Genev based on cross-section-weighting subject to constraints on W^2 and Q^2, discussed below. The predicted final-state particles were then boosted and rotated back to the lab frame by reversing all boosts and rotations done to the initial-state particles. In order to make effective use of simulated events without biasing distributions, those events which had a final electron azimuthal angle outside the range of -20° to $+20^\circ$ were rotated about the beam direction by an angle chosen to give a final azimuthal angle chosen randomly within that range. This enhanced the yield of events within the BigBite acceptance but didn't affect distributions which had, at minimum, a requirement of a hit in BigBite.

The range of Q^2 and W^2 to be generated by Genev was selected empirically since the effects of Fermi motion made it difficult to predict the significant range *a priori*. A low-statistics run of the simulation with a broad range was subjected to the acceptance cut of BigBite for the angle(s) of interest for the beam energy being simulated. The resulting Q^2 and W^2 distribution showed clear peaks in the regions which were relevant for scattering into BigBite. High statistics runs were then done with those ranges selected for generation of Genev events.

Full kinematic information was written out for each event (including particle identification for each four-vector). These were then selected to produce samples of interest for each kinematic point which would have an electron within the BigBite acceptance. The effects of finite detector resolution

were folded in (by smearing of each four-vector) before calculation of kinematic quantities of interest such as W^2 and θ_{pq}.

8.3 Inelastic Background Normalization

A fundamental difference between the quasi-elastic and inelastic simulations is that the inelastic simulation produced simulated events without a corresponding cross section by which to weight them. While the relative cross sections were accounted for in the probability of generation of different types and topologies of events, an overall normalization is needed to allow comparison of the inelastic events (from each target nucleon) with the quasi-elastic results.

Normalization of inelastic to quasi-elastic cross sections was done empirically, using SLAC spectra for single-arm electron scattering from the deuteron. Figure 15 shows spectra from [53] and [26] used for the normalization. The kinematic coverage of those measurements (truncated to the W^2 range of relevance) is shown in Fig. 16 with the same colors as in Fig. 15 to distinguish the two data sets. Two conveniently chosen ranges were used to characterize the cross sections in the quasi-elastic and inelastic regions. These are indicated in Fig. 15 as green bars indicating the limits selected for the "Quasi-elastic region" ($0.5 < W^2 < 0.88$ GeV^2) and red bars indicating the limits selected to define the "Inelastic region" ($1.3 < W^2 < 1.7$ GeV^2). As can be seen from the figures, the regions were chosen to give samples which were almost purely representative of the indicated final state, without significant contamination of inelastic events in the Quasi-elastic region or *vice versa*. The Inelastic region was also chosen close to the quasi-elastic peak so it would be representative of the events which would be likely to cause background.

Within the quasi-elastic model, the kinematic variation of cross-section within the Quasi-elastic region would be expected to follow the sum of the elastic cross sections for scattering from the proton and neutron. The numerically summed cross section in the Quasi-elastic region of each spectrum was divided by the predicted sum of proton-elastic and neutron-elastic (based on scaled-dipole and Galster) to obtain a measured strength (which was quite stable at a value of ≈ 0.35). Similarly, based on

$$\frac{d^2\sigma}{d\Omega dE'} = \frac{\alpha E'(W^2 - m_p^2)/(2m_p)}{4\pi^2 Q^2 E} \frac{2}{1-\epsilon}(\sigma_T(W^2, Q^2) + \epsilon\sigma_L(W^2, Q^2))$$

the kinematic factors were divided out of each bin of the double-differential cross section in the Inelastic region to yield the corresponding value of $(\sigma_T + \epsilon\sigma_L)$. Since the non-resonant background dominates over Δ production in these spectra, a non-resonant empirical scaling of $\sigma_L/\sigma_T \approx 0.25/\sqrt{Q^2}$ was used to allow σ_T (summed over the Inelastic region) to be extracted for each spectrum. (An alternate extreme would be to treat the inelastic cross section as purely transverse, as it might be if the Δ dominated. This was tried and resulted in only a modest change in the predicted inelastic strength at the the kinematics of interest.) The inelastic/quasi elastic strength can then be characterized as the ratio of the extracted σ_T from the Inelastic region divided by the scaled cross-section from the Quasi-elastic region. This ratio (for both sets of SLAC kinematics) was found to be reasonably well parameterized as a simple parabolic function of Q^2 ($r = 0.015\frac{Q^2}{(\mathrm{GeV/c})^2}$). This form was then used to predict the inelastic cross section within the Inelastic region for the Q^2 applicable for the beam energy and scattering angle of the kinematics of interest. These were found as multiples of the summed simulated cross section in the Quasi-elastic region (divided by the sum of proton and neutron elastic cross sections).

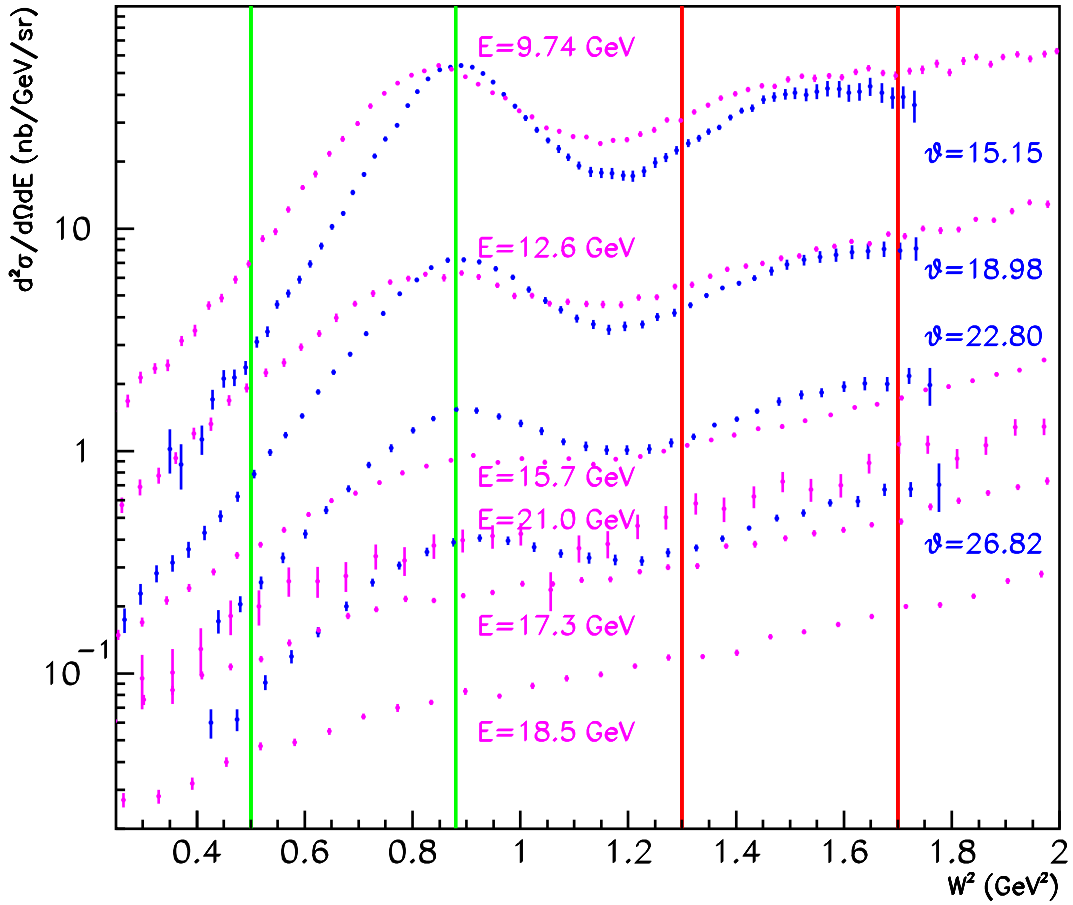

Figure 15: Measured single-arm spectra from SLAC covering the quasi-elastic and inelastic regions. Blue points were taken at E=5.507 GeV and indicated angle (in degrees). Magenta points were taken at indicated energy and $\theta = 10°$.

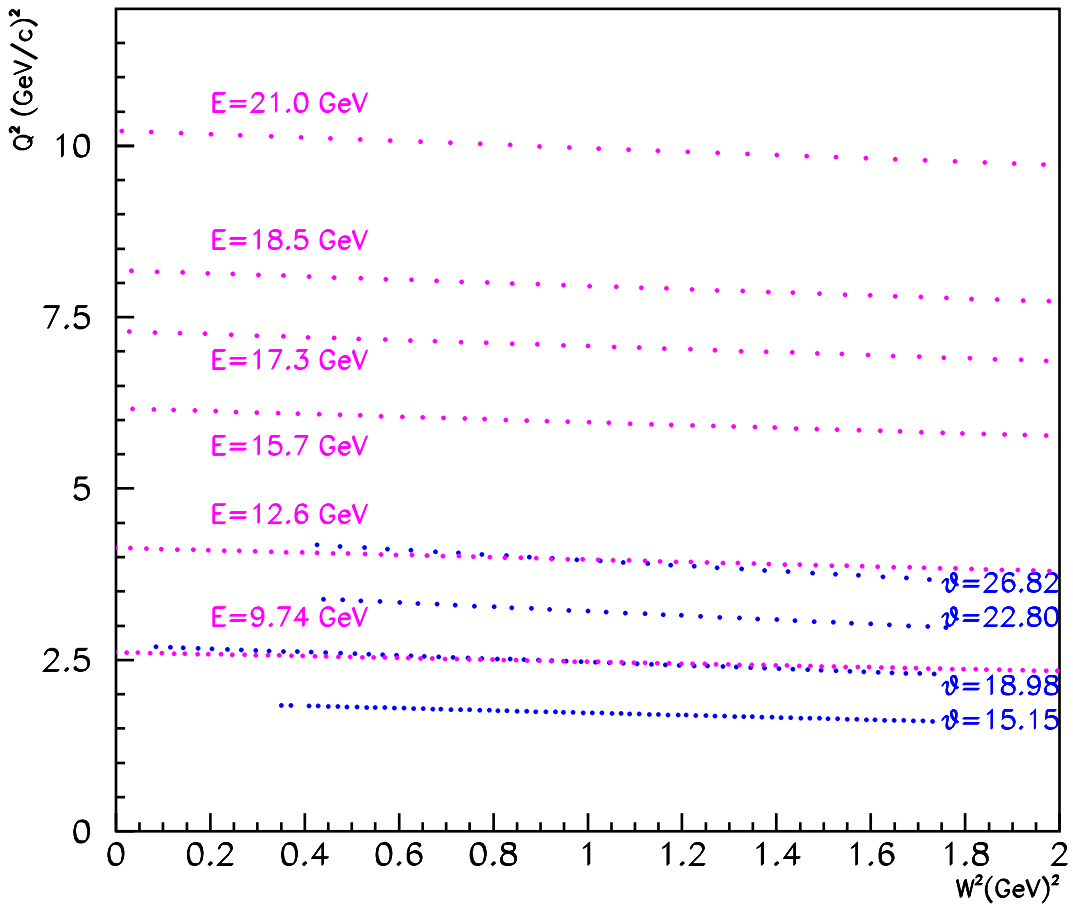

Figure 16: The Q^2 vs. W^2 coverage corresponding to the spectra of the previous figure.

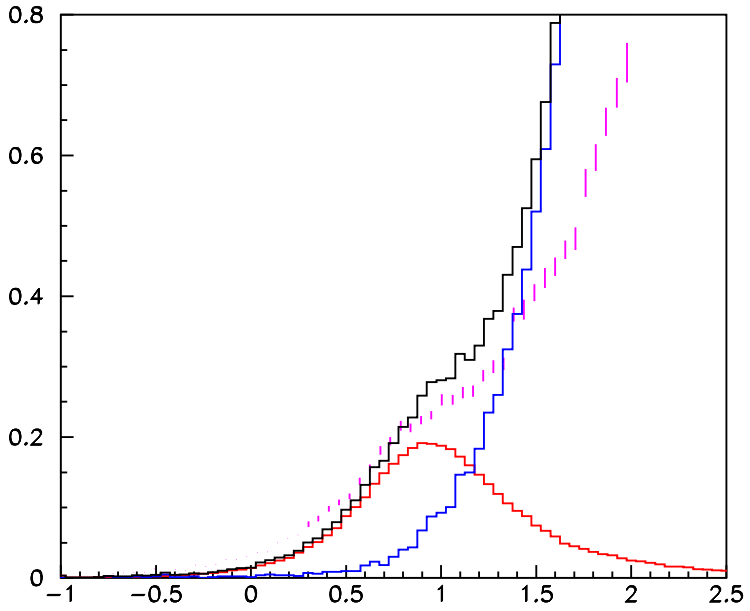

Figure 17: A measured spectrum [26] for single-arm electron scattering from deuterium (E=18.5 GeV, $\theta = 10°$) is compared to the Monte-Carlo prediction at the same momentum-transfer (the $Q^2 = 8$ point in the present proposal, at E=6.0 GeV, $\theta = 52.0°$). The data points are shown in magenta, the Monte-Carlo prediction in black. (The quasi-elastic contribution is shown in red, while the inelastic prediction is in blue.) **There are no adjustable parameters.** The Monte-Carlo spectrum has simply been scaled up by the ratio of (dipole-approximation) prediction for the ratio of deuteron quasi-elastic cross sections.

This gave the total normalization of the inelastic cross section. It remained to find individual scaling factors for the proton-target and neutron-target inelastic cross section to simulate the deuteron cross section. The inelastic cross section on the neutron was taken to be half of the inelastic cross section on the proton. Since the final state distributions (including individual measure of proton-coincidences or neutron-coincidences) were almost identical for the two assumed targets, the final results are almost insensitive to this choice of relative strength. This then allowed scaling factors to be determined to scale the number of simulated events to a double-differential cross section. These normalized results are shown in the next section.

A test of the Monte-Carlo at a previously calculated kinematic point ($Q^2 = 8$ (GeV/c)^2) is shown in Fig. 17. SLAC data [26] taken at a similar Q^2, but different beam energy and angle is compared to the Monte-Carlo prediction for single-arm electron scattering from deuterium. The SLAC data was taken at E=18.5 GeV and $\theta = 10°$. It is compared to the Monte-Carlo prediction at the same momentum-transfer at E=6.0 GeV and $\theta = 52.0°$. **There are no adjustable parameters.** The Monte-Carlo spectrum has simply been scaled up by the ratio of prediction for the ratio of deuteron quasi-elastic cross sections. This cross section was predicted (at each set of kinematics) as the sum of the dipole-prediction cross-section on the proton plus that on the neutron. The agreement is seen to be excellent and the inelastic background is, if anything, overestimated.

9 Inelastic Background

Results from the simulations of inelastic contributions are shown in Figures 18 through 21 for a selection of kinematic points across the range of interest. Each figure represents one of the kinematics shown in Table 1. The simulation was run for each kinematic point but typical example results are shown here for the for the $Q^2 = 3.5$, 8.5, 13.5 and 18 $(\mathrm{GeV/c})^2$ kinematic points.

In all simulated spectra, the statistical fluctuations reflect the statistics of the Monte-Carlo simulations and are not intended to simulate the statistics acquired by the proposed experiment.

The plots on the left in each figure show the neutron-coincident quasi-elastic (red) and inelastic (blue) spectra and their sum (black), integrated over the acceptance of the experiment. The plots on the right show the equivalent proton-coincident spectra. Proton- and neutron- coincidence here, as in the proposed experiment, are defined based on proximity of the simulated BigHAND hit to the position which would be predicted based on the $\vec{q}$-vector constructed based on the resolution-smeared information from BigBite.

The upper plots show the W^2 spectra Kinematic broadening and the large inelastic cross sections are seen to result in a large contribution of inelastic events under the quasi-elastic peak, particularly at high Q^2. (At the lowest Q^2 the apparently-large inelastic background is greatly reduced by the use of the fiducial cuts discussed above, leaving only the background spectra shown in green.) Without additional cuts to reduce this contamination, this would present a significant problem for these measurements.

The lower plots show the distributions of θ_{pq}. As mentioned above, θ_{pq} is the angle between direction of the nucleon's momentum ($\vec{p}$), reconstructed from the position of the hit on BigHAND, and the momentum-transfer vector ($\vec{q}$), as reconstructed based on the scattered-electron's energy and direction. For elastic scattering from a nucleon at rest, θ_{pq} would peak sharply at zero, having a finite width only due to measurement resolution. For quasi-elastic scattering, θ_{pq} is broadened by the unknown initial momentum of the struck nucleon. However, it is seen to still be sharply peaked. At the $Q^2 = 4.5$ $(\mathrm{GeV/c})^2$ point shown in Fig. 19, the quasi-elastic θ_{pq} distribution is seen to be almost entirely contained below $\theta_{pq} = 2^\circ$ while at the $Q^2 = 18$ $(\mathrm{GeV/c})^2$ point shown in Fig. 21, the quasi-elastic θ_{pq} distribution is even sharper, being almost entirely below $\theta_{pq} = 1^\circ$. The distribution for inelastic events is seen to be much wider. This provides an additional cut which can be used to select the quasi-elastic events of interest and reject the background from inelastic events. Furthermore, the linear rise of the inelastic distribution (which is a geometric effect, reflecting a roughly constant density of nucleon hits per unit area in the region pointed to by the $\vec{q}$ vector) suggests the possibility of correcting for residual inelastic contamination by extrapolating the large-angle θ_{pq} spectrum into the region of the cut and predicting the contribution of inelastic events surviving the cut.

From the figures presented above, it is clear that the inelastic background is largest in the case of neutron-coincident measurements at the highest Q^2. For this case, Fig. 22 presents additional results from the simulation demonstrating the effect of cuts on θ_{pq}. The signal-to-noise ratio is seen to improve as the cut is tightened. For a cut tighter than $\theta_{pq} < 1^\circ$ the accepted quasi-elastic coincidence cross section is seen to decrease (as expected from the θ_{pq} plot shown in Fig. 21).

The optimal choice of cuts on W^2 and θ_{pq} involves a trade-off of statistics against signal purity. Integration of the spectra for the $\theta_{pq} < .5^\circ$ cut, for example, indicates that the inelastic background can be reduced to a 23% contamination by a cut selecting $-0.95 < W^2 < 0.5$ GeV^2 at a cost of 77% of the quasi-elastic acceptance. The signal could be about doubled by increasing the upper W^2

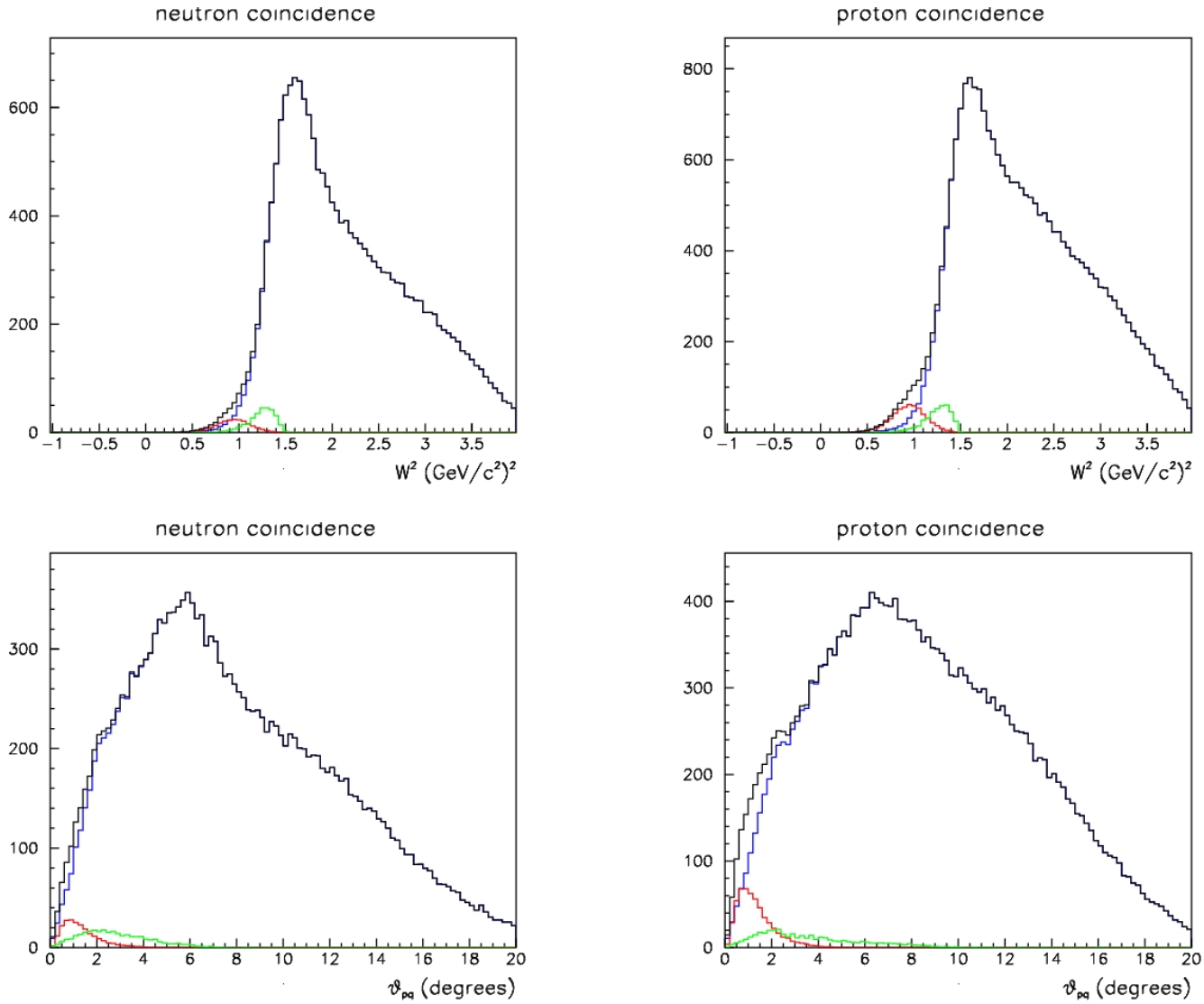

Figure 18: Projections onto W^2 and θ_{pq} for simulations of inelastic background (blue) and quasi-elastic (red) cross section for the $Q^2 = 3.5$ (GeV/c)^2 kinematic point. Vertical axes are efficiency- and acceptance-weighted cross section integrated over the combined spectrometer acceptance, in fb/bin. The effect of applying the tight fiducial cuts on the inelastic background is shown by the green curves.

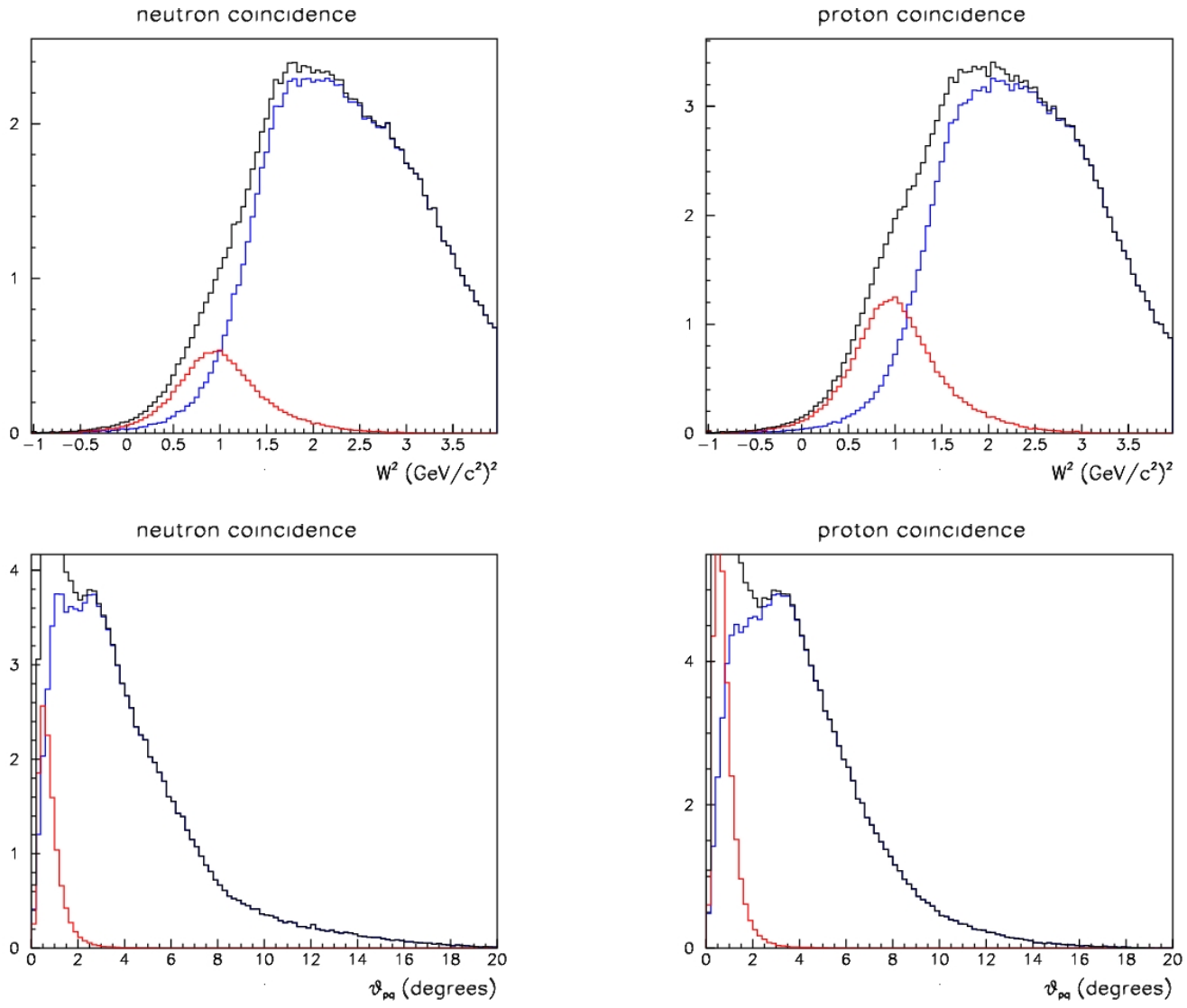

Figure 19: Projections onto W^2 and θ_{pq} for simulations of inelastic background (blue) and quasi-elastic (red) cross section for the $Q^2 = 8.5$ (GeV/c)^2 kinematic point. Vertical axes are efficiency- and acceptance-weighted cross section integrated over the combined spectrometer acceptance, in fb/bin.

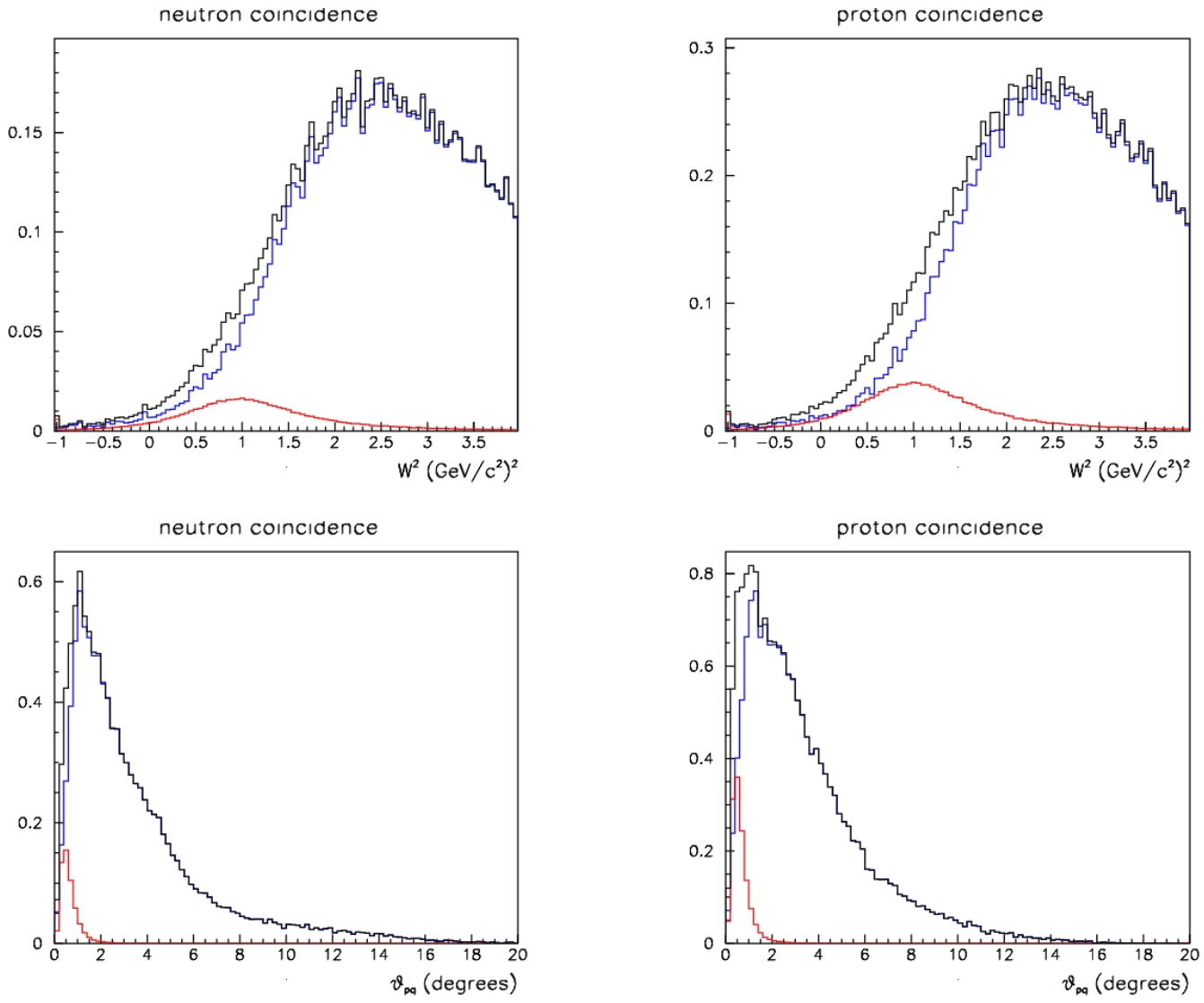

Figure 20: Projections onto W^2 and θ_{pq} for simulations of inelastic background (blue) and quasi-elastic (red) cross section for the $Q^2 = 13.5$ (GeV/c)^2 kinematic point. Vertical axes are efficiency- and acceptance-weighted cross section integrated over the combined spectrometer acceptance, in fb/bin.

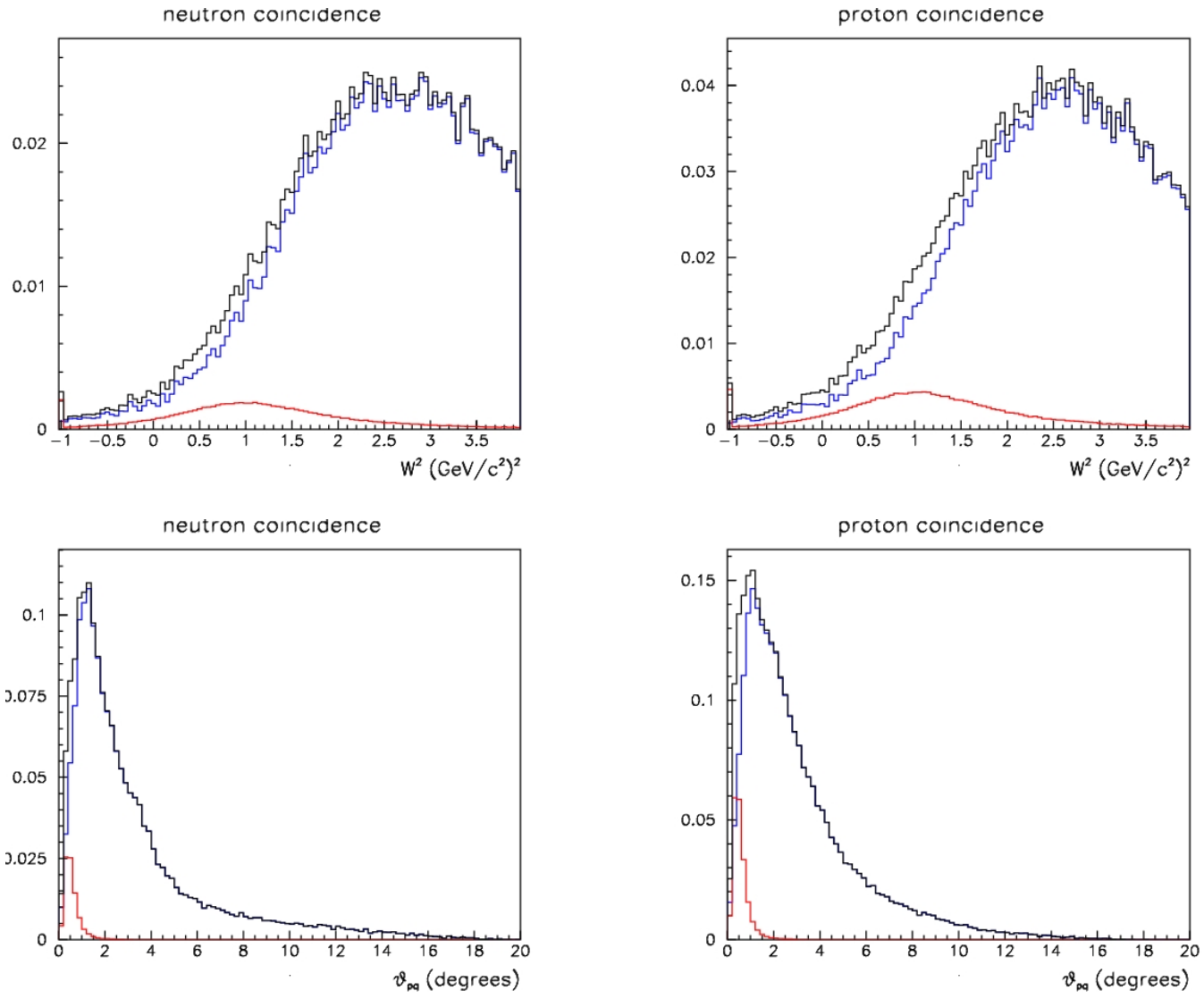

Figure 21: Projections onto W^2 and θ_{pq} for simulations of inelastic background (blue) and quasi-elastic (red) cross section for the $Q^2 = 18$ (GeV/c)^2 kinematic point. Vertical axes are efficiency- and acceptance-weighted cross section integrated over the combined spectrometer acceptance, in fb/bin.

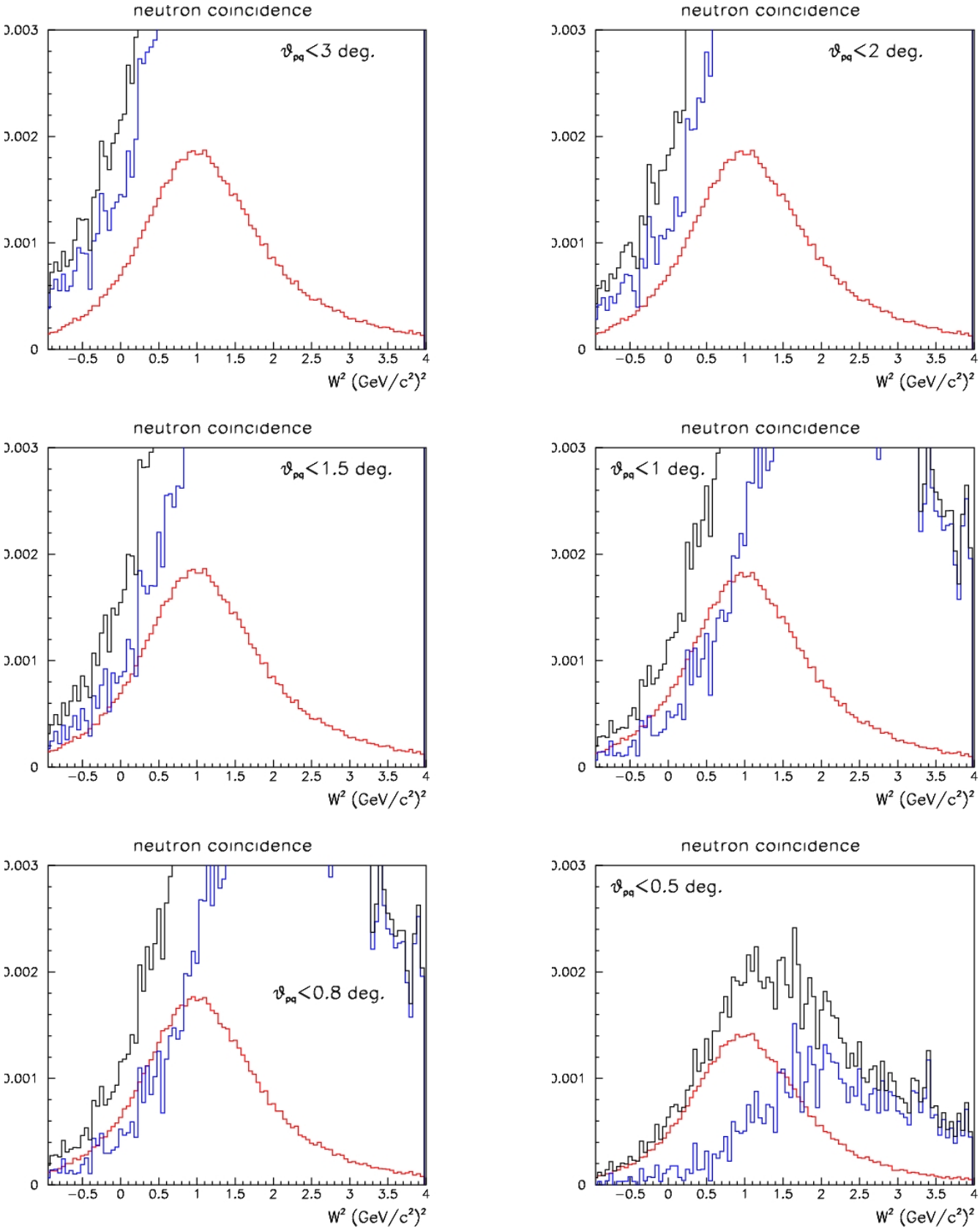

Figure 22: Quasi-elastic (red) and inelastic (blue) cross-section vs. W^2 with coincident neutron detection with different cuts on θ_{pq}. The cuts applied to θ_{pq} are indicated on each plot. The vertical axis for each plot is the efficiency- and acceptance-weighted integrated cross section in fb/bin.

Table 5: Estimated fractional contamination of inelastic events in the quasi-elastic sample after W^2 and θ_{pq} cuts but *before any correction is applied*

Q^2 (GeV/c)^2	3.5	4.5	6.0	8.5	10.	12.	13.5	16.	18.
Max. θ_{pq} (deg.)	2.5	2.3	1.9	1.1	0.9	0.8	0.7	0.6	0.6
Max. W^2 (GeV^2)	1.1	1.2	1.3	1.3	1.4	1.4	1.6	1.6	1.7
Proton contamination (%)	5.3	5.5	8.8	13.	15.	21.	26.	28	33.
Neutron contamination (%)	13.5	11.	15.4	26.	30.	34.	43.	50.	51.

cut-off to 1.0 GeV^2 while only increasing the background to 26%. Similarly increasing the cut-off to 1.5 GeV^2 would add another 50% to the integrated signal but would increase the background contamination to 37%. (We refer to background contamination at background/signal. The fraction of background relative to total counts would be a smaller number. e.g. A 50% background, meaning that background is 50% of signal, is equivalent to 33.3% of total events being background events.)

The best cuts will have to be chosen based on the observed data, estimated background contamination and estimated systematic error on the determination of the background. For the simulated data presented here, a set of cuts was chosen to minimize the error on the extracted value of R. These were based on the simulated spectra, the anticipated luminosity and running time requested in the present proposal, and an assumed 20% systematic error (in addition to $\sqrt{n}$ statistical error) on the background contamination. The fractional systematic error was assumed to be common in the neutron and proton contamination and so partly canceled in the evaluation of R. For the actual analysis, a locus in $W^2 - \theta_{pq}$ space might be used to select events. For the purpose of rate estimates, a simple rectangular region was selected by optimizing separate cuts on W^2 and θ_{pq}.

The resulting optimal cuts and anticipated contamination are presented in Table 5. These results are used below in estimation of systematic errors. The contamination fractions listed in Table 5 are the values before correction. Given a 20% systematic error, the majority of the contamination would be subtracted off. Since the inelastic backgrounds in the neutron and proton spectra are expected to be of similar shape (and will be extrapolated into the quasi-elastic region using similar shapes) if one background is underestimated the other may also be expected to be underestimated. Similarly, if the neutron background is oversubtracted, the proton background will also be oversubtracted. As mentioned above, this common error in the numerator and denominator partly cancels in evaluation of the ratio, R''. The cancellation is not complete because the fractional errors in the numerator and denominator will differ. But the partial cancellation results in a fractional error on the ratio, due to systematic background error, which is smaller than the fractional error contributed to the neutron or proton counts.

10 Rates and Trigger

In this section we review the inputs used in the rate calculations and give the expected rates for the quasi-elastic coincidence measurements and for the calibration reactions.

Since background rates are roughly proportional to the number of target nucleons, rate estimates are based on a luminosity of $\mathcal{L} = 6.7 \times 10^{37}/A$ cm^{-2}s^{-1}, where A is the number of nucleons in the

Table 6: Suitable thresholds for the electromagnetic calorimeter trigger are listed. For comparison, the lower limit for quasi-elastically scattered electrons is also given.

Q^2	3.5	4.5	6.0	8.5	10.	12.	13.5	16.	18.
Quasi-elastic E'_{min} (GeV)	2.4	1.8	1.1	1.8	3.0	2.0	1.4	2.1	1.2
Threshold (GeV)	2.1	1.6	1.0	1.6	2.7	1.8	1.2	1.9	1.0

target. While this exceeds our experience in the GEn experiment [43] using the same equipment, there are several factors which decrease the susceptibility of the present experiment to accidental background. The observed rate of accidental events above threshold in BigHAND was ≈ 2 MHz for that measurement. BigHAND will be significantly further back from the target (17 m compared to 6.5 to 12 m for GEn running) so a much smaller solid angle is subtended. Further, the deflector magnet will reduce rates due to low-energy particles. BigBite will be instrumented with GEM detectors which should be able to handle a significantly higher luminosity than proposed here.

A Monte Carlo [44] simulation has been done to predict the background trigger rates which will may be expected as a function of the threshold applied to the electromagnetic calorimeter. The simulation included a parameterization of expected light-generation by hadrons. Pion rates were based on an empirical fit to observed charged pion production rates measured at SLAC. A parameterization of electron-scattering rates from deep inelastic scattering was also included. The results of the simulations at the kinematic points of this experiment are shown in Fig. 23. For each kinematic point, the threshold must be chosen chosen low enough so that quasielastic events are accepted with reasonable efficiency. An advantage of the ratio method is that there is no systematic error introduced by such an inefficiency since it would be independent of the type of recoiling nucleon. Table 6 lists, for each kinematic point, the lower limit for scattered-electron energy for quasielastic events, as determined from the quasi-elastic Monte Carlo. The table also lists suitable threshold values which are $\approx$10% below this minimum. Comparing those thresholds to Fig. 23 shows that the expected background trigger rates are comfortably low, generally well below 1 kHz.

The threshold on the electromagnetic calorimeter will serve to reduce the trigger rate due to low energy scattered electrons from inelastic events. While suppression of inelastic events is generally advantageous, it is necessary to have a measure of the inelastic rate near the quasi-elastic peak in order to test and calibrate inelastic predictions which can then be used to correct for contamination under the quasielastic peak. Monte Carlo simulations of the effect of a threshold-cut on scattered electron energy have determined that these thresholds will cause negligible distortion of the inelastic background for $W^2 < 2.5$ (GeV/c)^2.

For all rate calculations the track-reconstruction efficiency in BigBite was taken to be 75% and the trigger live time was taken to be 80%. The estimated efficiencies for neutron and proton detection (shown in Fig. 7) are given in Table 7.

The cross section for quasi-elastic scattering was numerically integrated over the combined acceptance of BigBite and BigHAND, subject to the fiducial cut, as described in section 8.1. The integrals, labeled as "$\int \frac{d\sigma}{d\Omega} d\Omega$", are given in Table 7. The line labeled "W^2/θ_{pq} cut" gives the fraction of quasi-elastic events surviving the cuts, described in the previous section, used to reject inelastic events. Defining $\mathcal{L}_0 = 6.7 \times 10^{37}$ cm^{-2}s^{-1} = 240/fb/hr, the luminosity for the quasi-elastic measure-

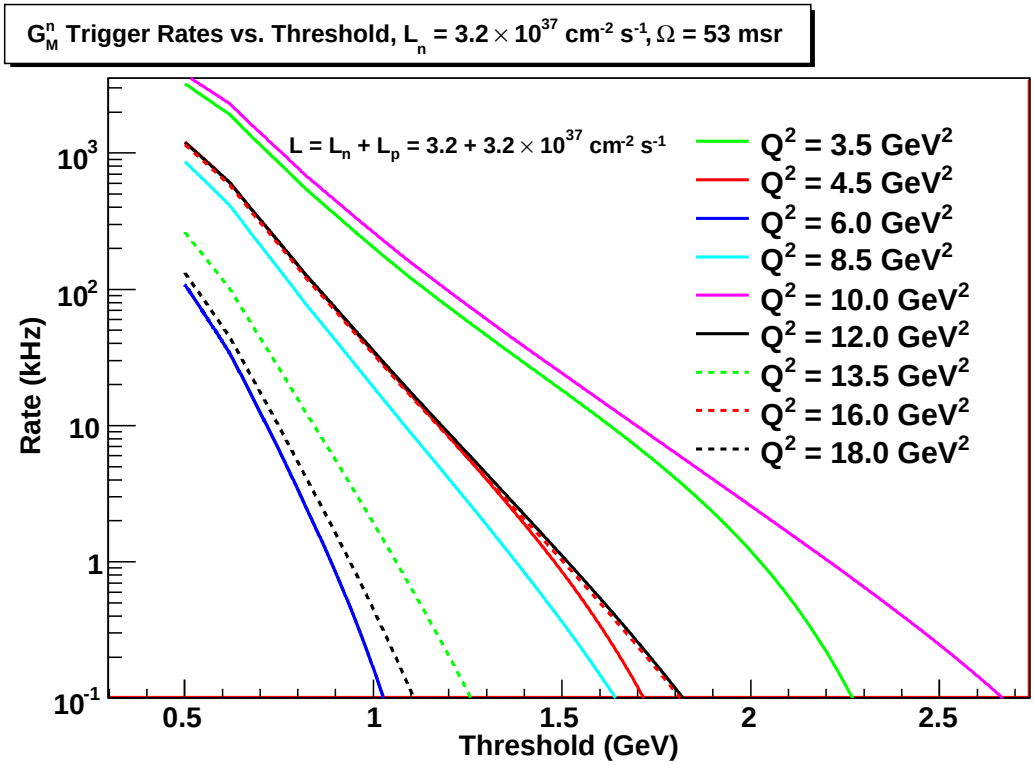

Figure 23: The predicted trigger rates from background particles as a function of the threshold applied to the electromagnetic calorimeter. Each curve represents one of the proposed kinematic points.

Table 7: Values used in calculating count rates.

Q^2 (GeV/c)^2	3.5	4.5	6.0	8.5	10.	12.	13.5	16.	18.
E (GeV)	4.4	4.4	4.4	6.6	8.8	8.8	8.8	11.	11.
θ_e	32.5°	41.9°	64.3°	46.5°	33.3°	44.2°	58.5°	45.1°	65.2°
p efficiency (%)	78.4	86.0	93.8	98.2	96.5	99.0	99.0	99.0	99.0
n efficiency (%)	73.0	80.9	86.6	86.6	91.3	91.1	91.1	91.1	91.1
Quasi-elastic									
p-coinc. $\int \frac{d\sigma}{d\Omega} d\Omega$ (fb)	890	570	69	30.4	32.	5.9	1.35	1.21	.20
n-coinc. $\int \frac{d\sigma}{d\Omega} d\Omega$ (fb)	380	250	31	13.9	15.	2.7	0.63	0.56	.093
W^2/θ_{pq} cut (%)	80	85	74	67	64	61	63	60	63
Proton elastic (calibration)									
Full $\Delta\Omega$ (msr)	22.6	38.4	53.6	—	—	—	—	—	—
$\frac{d\sigma}{d\Omega}_{p(e,e')}$ (pb/sr)	107	17	1.3	—	—	—	—	—	—
$p(\gamma,\pi^+)n$ (calibration)									
$\int \Gamma dk$	0.0023	0.0030	.0046	—	—	—	—	—	—
$\theta^*_{\gamma\pi}$	86.5°	102°	128°	—	—	—	—	—	—
$\frac{d\sigma}{d\Omega}_{p(\gamma,\pi^+n)}$ (pb/sr)	2100	1190	1770	—	—	—	—	—	—

ments on deuterium will be $\mathcal{L}_0/2 = 120$/fb/hr. The resulting predicted rates of electron-nucleon coincidences are given in the first two lines of Table 8.

For proton efficiency measurements using elastic scattering on Hydrogen, the full combined solid angle of BigBite and BigHAND can be used, without a fiducial cut. This is given as "Full $\Delta\Omega$" in Table 7. The (scaled dipole approximation) cross section is also given. For this calibration on an LH2 target, the full luminosity $\mathcal{L}_0$ can be used. The resulting rates are given in the third line of Table 8. Dashes indicate the kinematic points for which proton efficiency is high and will be estimated rather than based directly on calibration runs.

For the neutron efficiency measurements using the $p(\gamma,\pi^+n)$ reaction the full combined solid angle, "Full $\Delta\Omega$" can again be used. Because the 6% radiator will approximately quadruple the reaction rates in the target, the luminosity must be reduced to $\mathcal{L}_0/4$. Table 7 gives the number of useful end-point photons per incident electron ($\int \Gamma dk$), from Table 4. Dashes indicate the kinematic points for which neutron efficiency is high and will be estimated rather than being based directly on calibration runs. Table 7 also lists the center of mass angle, $\theta^*_{\gamma\pi}$, for the (γ,π^+) reaction and the estimated cross section for the reaction. The latter is calculated using the scaling predicted by the constituent counting rule:

$$s^7 \frac{d\sigma}{dt} = \text{ constant}$$

where s and t are the Mandelstam variables (invariant mass squared and four-momentum transfer squared). The constant value was conservatively taken to be 0.5×10^7 GeV^{14} nb/GeV^2 at $\theta^*_{\gamma\pi} = 90°$ based on measurements [54] made in the range of s of interest. The cross section for the actual $\theta^*_{\gamma\pi}$

Table 8: Predicted coincidence rates (counts per hour)

Q^2 (GeV/c)^2	3.5	4.5	6.0	8.5	10.	12.	13.5	16.	18.
$d(e,e'p)$	40700	26600	3110	1345	1240	244	56.7	47.0	7.9
$d(e,e'n)$	17600	12000	1600	627	580	114	26.5	22.0	3.72
$p(e,e'p)$	273000	82000	9300	4400	5000	850	200	175	30
$p(\gamma,\pi^+n)$	2920	4030	13500	—	—	—	—	—	—

was then found based upon an empirical fit [55] to the angular distribution:

$$s^7\frac{d\sigma}{dt} \propto (1-\cos\theta^*_{\gamma\pi})^{-5}(1+\cos\theta^*_{\gamma\pi})^{-4}$$

Finally $\frac{dt}{d\cos\theta}$ was numerically evaluated to convert from $\frac{d\sigma}{dt}$ to $\frac{d\sigma}{d\Omega}$. The resulting estimated count rates are given in the last line of Table 8.

11 Systematic Errors

In this section we will estimate (or set upper limits on) contributions to the systematic error on the ratio R determined by this experiment. This sets the scale for the statistical accuracy for which we should aim since there would be little gain in achieving statistical errors which are much smaller than the systematic errors.

The use of the ratio method eliminates many potential sources of systematic error. Because $d(e,e'p)$ and $d(e,e'n)$ are measured simultaneously, their ratio is insensitive to target thickness, target density, beam current, beam structure, live time, trigger efficiency, electron track reconstruction efficiency, etc. So the fractional error achieved on the ratio can be much smaller that which could be achieved on the measurement of either cross section in itself.

Table 9 lists the estimated contributions to systematic errors, which are discussed in detail below.

The corrections needed to convert from the measured value R'' (Equation 1) to the quantity of interest, R (Equation 2) are only of the order of 1%, so systematic errors on them will be neglected.

The errors on the proton elastic cross section (needed to extract G_M^n from R) do not contribute to the error on the ratio G_M^n/G_M^p . This is a more fundamental result than G_M^n, itself, or the ratio of G_M^n to the scaled dipole. The ratio G_M^n/G_M^p is generally more directly calculable within a given theoretical model. While subsequent improvements in proton cross section measurements can be combined retrospectively with the R values from this experiment to improve the extraction of G_M^n, we include an estimated contribution to the error based on projected errors on G_M^n/G_M^p from an approved 12 GeV experiment [50]. We assume a 1.7% fractional error on the proton cross section across the region of interest except 4% at the highest Q^2, which is beyond the region to be covered in that measurement. This error should be included as a systematic in extraction of $(G_M^n)^2$, but not of the ratio G_M^n/G_M^p .

If G_E^n behaves like the Galster parameterization at high Q^2, then its contribution to the neutron cross section is small. Thus, even large fractional errors in G_E^n would produce only small errors in

Table 9: Estimated contributions (in percent) to systematic errors on R.

Q^2 (GeV/c)^2	3.5	4.5	6.0	8.5	10.	12.	13.5	16.	18.
proton cross-section	1.7	1.7	1.7	1.7	1.7	1.7	1.7	1.7	4.
G_E^n	1.7	1.1	0.49	0.51	0.56	0.69	0.38	.89	.39
Nuclear correction,	-	-	-	-	-	-	-	-	-
Accidentals	-	-	-	-	-	-	-	-	-
Target windows	.2	.2	.2	.2	.2	.2	.2	.2	.2
Acceptance losses	0.45	0.5	0.3	0.4	0.16	0.18	0.1	0.1	.08
Inelastic contamination	1.5	1.14	1.32	2.64	2.94	2.62	3.24	4.4	3.64
Nucleon mis-identification	0.6	0.6	0.6	0.6	0.6	0.6	0.5	0.5	0.5
BigHAND calibration	0.3	0.3	0.5	2	2	2	2	2	2
Without proton err.									
Syst. error on G_M^n/G_M^p	1.21	0.9	0.81	1.72	1.83	1.72	1.93	2.47	2.1
With proton err.									
Syst. error on G_M^n	1.48	1.24	1.17	1.92	2.02	1.91	2.11	2.61	2.9

$(G_M^n)^2$. The contribution listed as G_E^n in Table 9 are based on an assumed error of 100% of the Galster parameterization, growing to 200% for $Q^2 = 10$ (GeV/c)^2 and growing to 400% for the two highest-Q^2 points.

Accidental coincidences of background events in BigHAND are not expected to cause significant systematic errors. Previous experience in the GEn experiment [43] showed a background rate of ≈2 MHz across the entire detector at a similar luminosity (BigHAND saw about half the proposed luminosity, although BigBite viewed only a third of that). BigHAND will be significantly further from the target for this measurement so lower rates may be expected. Even with a 1 MHz rate, the probability of an accidental coincidence within a 5 ns timing gate will be only 0.5% across the entire detector. The area searched for coincident protons or neutrons is limited by the $\theta_{pq} < 2^\circ$ cut to about 1.1 m^2 of the 8.4 m^2 face. So the rate of accidental coincidences is expected to be less than 0.07% for each nucleon species. Furthermore, this accidental contamination can be accurately estimated and subtracted by measuring the accidental coincidence rate in other parts of BigHAND, where true coincidences are not expected.

The target windows contain about 3.4% as many nucleons as the LD2 target. We use this as an upper limit on the background contribution since many of the events from aluminum will be rejected by the $\theta_{pq} < 2^\circ$ cut. This contribution will be subtracted off by running on a dummy target with thick aluminum windows. It should be possible to apply this correction with at least 5% accuracy (allowing for uncertainty in window thickness). So the systematic error on the correction should be under 0.17%.

11.1 Acceptance Losses

As discussed above, loss of nucleons from the acceptance of BigHAND can cause a systematic error, to the extent that the losses differ for neutrons and protons. At the higher Q^2 points, the

distribution of nucleons (shown in Fig. 12) are centered in BigHAND, with only modest acceptance losses. At the lower Q^2 points a fiducial cut will be applied to select events which are similarly centered in BigHAND (as discussed in section 6) so the acceptance losses are kept small. The acceptance corrections are less than 5% in all cases, and considerably smaller at the highest Q^2 points. These losses result from the high momentum tail of the deuteron wave-function, which is identical for the neutron and proton. The cause of a difference in the corrections for the two nucleon species would be a difference in placement of the proton and neutron 'images' relative to the edges of BigHAND. It very conservative to allow for a possible 10% uncorrected difference in these corrections. This is entered as the systematic error contribution in Table 9.

This systematic error can be investigated (and perhaps even reduced) by examining the stability of the extracted ratio, R, as the fiducial cut is tightened or loosened from its normal value. Additionally, choosing a "window-frame" fiducial which preferentially selects events scattered near the edge of the BigHAND acceptance would allow investigation of the actual loss of protons and neutrons, which can be compared to Monte-Carlo estimates. Perhaps more importantly, such a study can be used to determine how closely the fractional losses of neutrons and protons are matched.

11.2 Inelastic Contamination

With the W^2 cuts described at the end of section 9 the predicted residual contamination of inelastic events in the quasi-elastic sample *before any corrections are made* are given in Table 5. These may be overestimated since the kinematics used for the inelastic simulation tend to exaggerate the effects of Fermi broadening. In the ratio R the contamination tends to cancel. More importantly, it should be possible to accurately estimate and subtract the inelastic contamination. The θ_{pq} distribution (such as that shown in Fig. 21) beyond 2° gives a measure of the amount of inelastic contamination. The measured distribution can be extrapolated to small angle to estimate the residual contamination. It should certainly be possible to estimate the inelastic contamination at the 20% level. Assuming the numbers in Table 5 are reduced by such a factor, gives the contributions listed in Table 9. This is generally the largest contribution to the systematic error.

11.3 Nucleon mis-identification

Because of the long tail of the momentum distribution of the deuteron wave-function, some nucleons will be displaced far from the position predicted based on their $\vec{q}$ vector and charge. This will result in mis-identification if a neutron is displaced sufficiently far upwards or a proton sufficiently far downwards. In the model used for the deuteron wave-function, about 5% of the nucleons have a component of momentum exceeding 100 MeV/c in any chosen direction. With a 200 MeV/c 'kick' being given to protons by the dipole, this would result in 5% mis-identification rates. The cut on W^2 preferentially rejects events with large Fermi momentum, however and so the mis-identification rate is reduced to 3% or less for the cuts considered here. The misidentification of one species as the other and *vice versa* do not cancel because the proton rate is higher and protons have a higher efficiency of being detected. If the mis-identification went uncorrected, the number of detected 'neutrons' would be increased by proton contamination while the number of detected 'protons' would be decreased by a loss of protons which would not be offset by misidentified neutrons. Thus the effect would be an overestimate of R. The fractional overestimate of R depends on the actual ratio of proton/neutron cross sections and efficiencies. Taking the ratio of cross sections to be

$\frac{d\sigma}{d\Omega}\big|_p$ / $\frac{d\sigma}{d\Omega}\big|_n \approx 2.4$ and the detection efficiencies to be $\epsilon_p = 80\%$ and $\epsilon_n = 75\%$, this 3% kinematic spread of nucleons would cause the neutron rate to be overestimated by 4.7% and the protons to be underestimated by 1.8% and so R would be overestimated by 6.6%.

The contamination will not go uncorrected, however, and at least two techniques will be used to measure this kinematic tail. The neutron tail below the predicted point on the face of BigHAND can be measured without contamination from protons. Similarly the proton tail above the predicted point on BigHAND will be free of neutrons. Symmetry can then be used to predict the contamination of neutrons in the proton peak and, with minor kinematic corrections because of the deflection magnet, the proton contamination of the neutron peak. Since these tails originate from the same Fermi motion, the neutron and proton tails should be almost identical apart from minor distortion due to the deflection magnet. Another technique for determining the tails in the 'contamination region' will be to use the vetos to preferentially select neutrons or protons. In particular a clean sample of neutrons can be selected (with only a few percent proton contamination, which can be subtracted off) to separately determine the kinematic spread. It should be possible to measure at the 10% level, the 'leakage' of neutrons/protons into the regions in which the other species is expected. A 10% error in the measurement of such a 3% tail would cause a systematic error of ≈0.6% in the extracted value of R. In fact, stronger field settings used for higher-Q^2 points should reduce the misidentification, so the error estimates in Table 9 are probably significantly overestimated.

11.4 Nucleon Detection Calibration

There are several potential issues involved in determining the systematic errors associated with the calibration of the BigHAND efficiencies for detection of neutrons and protons. A useful attribute of the $p(\gamma, \pi^+)n$ reaction is that the neutrons used for calibration have essentially the same energy as those in the middle of the quasielastic peak. This is a significant advantage relative to our previous CLAS experiment [37,39] at lower Q^2 in which $p(e, e'\pi^+)n$ was used for calibration. There, the three-body final state gave lower neutron energies than those of interest so it was necessary to parameterize the efficiency as a function of energy to estimate the efficiency at the energy of interest. Thus, the largest source of systematic errors in the earlier experiment is avoided here.

In principle the statistical error on the calibration of the detection efficiencies represents a systematic error on the measurements of the quasi-elastic reaction of interest. In fact it is not prohibitive to obtain sufficient statistics on the calibration reaction so that the error on the efficiencies are comparable to the statistical error on the quasi-elastic measurements. We treat this as a statistical error in subsequent discussions, and so don't include it in Table 9.

As shown in Table 3, up to 17% of the quasi-elastic nucleons (in the $Q^2 = 6.0$ (GeV/c)^2 case) will fall outside the region which can be calibrated at elastic kinematics at the same beam energy and BigHAND position. The "uncalibrated" regions of the detector could reasonably be assigned the average efficiency obtained from the calibration, since they share the same shower-generation geometry and are, in fact, mostly just different positions on the same physical detector bars. A further refinement can be made, as has been described in section 7.3, by extrapolating calibrations made at lower energies to take into account the slightly different interaction probability. Since the efficiency is high, and unlikely to change rapidly, it is unreasonable to expect the efficiency in the "uncalibrated" region to differ by more than 2% from the efficiency predicted by these methods. (Copious calibration data will be taken at the low Q^2 point, so any anomalous regions, such as dead PMT's will be identified and either repaired or corrected for.) We assign an upper-limit systematic

error of 2% of the fraction of the events which fall outside the calibrated region. Since this error appears in both the numerator and denominator of R, it is multiplied by $\sqrt{2}$.

For the highest-Q^2 points, no direct calibrations will be made. The proton and neutron efficiencies there are both large and stable, we assign a systematic error 2% in the efficiency correction for those points.

The final line of Table 9 shows the estimated total systematic error on R, found by adding the individual contributions in quadrature.

12 Installation

All the equipment used for this experiment is either already existing or planned for use in the Super-BigBite-Spectrometer (SBS) in Hall A.

- The BigBite spectrometer exists, but with different tracking instrumentation than is planned for this measurement.
- The GEM detector planes are planned as instrumentation of the polarimeter in the SBS
- The BigHAND detector array exists and has been used in Hall A. It is presently in storage at JLab
- The BigBen magnet is needed for an already-approved [56] 12 GeV experiment. Although we are using it only as a deflector magnet, it will eventually be the heart of the SBS.

Two major pieces of equipment will need to be installed in the Hall for this experiment.

Since the BigHAND nucleon detector has been used in the past [43], there is operational experience on rigging it in and out of the Hall. In preparation for the GEn experiment, it was rigged into the Hall in six weeks, with no previous operational experience and with the BigBite spectrometer being rigged in parallel.

The 48D48 (BigBen) 'spectrometer' magnet (here being used as a particle-identification magnet) is available from BNL but will required major modifications in advance of installation to allow it to be placed close to the beam line without mechanical or magnetic interference with the beam on its way to the beam dump. We expect to play a leading role in the magnetic and mechanical design for modifications to the magnet and for beam line shielding and/or correctors. We will also participate in the design of mechanical systems to allow the magnet to be re-positioned for different scattering angles. These modifications are needed independently for the approved GEP [56] experiment.

The same equipment is needed for the proposed high-Q^2 measurement of G_E^n [40] and the BigBen magnet would be used for the proposed transversity experiment and as part of the SBS facility. Installation time could be economized by scheduling the G_E^n experiment to follow the presently proposed experiment. Then only the polarized ^{3}He target would need to be installed for the change-over to the next experiment. Similarly the BigBen magnet could then be instrumented to form the SBS spectrometer for the transversity measurement. This would obviate the need for rigging the magnet back out of the Hall.

A significant upgrade of the BigHAND electronics is planned, to reduce the dead time of the veto detectors. That can be carried out independently of Hall operations.

Table 10: Estimated statistical and systematic (from background subtraction only) errors on R for $W^2 - \theta_{pq}$ cuts optimized for the requested running times.

Q^2 (GeV/c)^2	3.5	4.5	6.0	8.5	10.	12.	13.5	16.	18.
Statistical (%)	0.3	0.3	0.8	1.4	1.3	2.4	3.2	3.4	5.9
Systematic (%)	1.5	1.2	1.3	2.6	2.9	2.6	3.2	4.4	3.6

Based on past experience, including the installation of the GEn experiment, we estimate that six to eight weeks will be required to install the equipment needed for this experiment. Ideally, of course, this will be carried out during an accelerator down-time, or when beam is unavailable because the three other halls are running.

13 Beam Time Request

Given the simulation results for rate estimates and background contamination, an evaluation was made of the trade-off of statistical and systematic errors. Since the dominant systematic error is due to background contamination, that was the error considered in choosing running times which allowed a good trade-off of cuts which were tight enough to reduce systematic errors but not so tight as to require prohibitive running times. Table 10 gives the resulting contributions of statistical errors and background-related systematic errors to the determination of R for the requested beam times listed below, in Table 11.

Table 10 demonstrates that the beam hour requests have been chosen to give a reasonable match of systematic and statistical errors. The four lowest-Q^2 points appear to be exceptions to this, with statistical errors which are significantly smaller than the systematic errors. Decreasing the running times at those kinematics to match the statistical and systematic errors would have only a very minor impact on the overall beam time request. The run times have been chosen to take advantage of the high rates and allow copious statistics to be accumulated to enable careful studies of small systematic effects using the data.

Because binomial statistics apply for the efficiency measurements, the number of required events is considerably smaller than might be expected for Poisson statistics. If N_{in} particles are incident on the detector, each with probability p of being observed, then the variance on the number of observed particles N_{obs} is

$$\sigma^2 = N_{in}\ p(1-p) \approx N_{obs}\ (1-p)$$

So the fractional error in the efficiency $\eta = N_{obs}/N_{in}$ is

$$\frac{\sigma_\eta}{\eta} = \frac{\sigma}{N_{obs}} = \frac{\sqrt{1-p}}{\sqrt{N_{obs}}}$$

The required statistics for a given fractional error is therefore reduced by a factor of $(1-p)$ compared to counting statistics. With conservatively estimated neutron and proton efficiencies of at least $p_n = 0.70$ and $p_p = 0.75$ this reduces the required number of calibration coincidences by factors of 0.3 and 0.25, respectively.

Table 11: Beam Time Request (beam hours). "Normal $\mathcal{L}$" refers to running at the standard luminosity of 6.7 $\times 10^{37}$ /A/cm^2/sec. Reduced luminosity running is indicated as "Half $\mathcal{L}$" or "10% $\mathcal{L}$".

Q^2 (GeV/c)^2	3.5	4.5	6.0	8.5	10.	12.	13.5	16.	18.	
E (GeV)	4.4	4.4	4.4	6.6	8.8	8.8	8.8	11.	11.	
θ_e	32.5°	41.9°	64.3°	46.5°	33.3°	44.2°	58.5°	45.1°	65.2°	
θ_N	31.1°	24.7°	15.6°	16.1°	17.9°	13.3°	9.8°	10.7°	7.0°	
d(e,e')										
Normal $\mathcal{L}$	12	12	18	18	24	36	96	108	216	
Dummy target	2	2	2	2	3	4	8	8	16	
Half $\mathcal{L}$	12	12	12	12						
Dummy half $\mathcal{L}$	2	2	2	2						
10% $\mathcal{L}$	12	12								
Dummy 10% $\mathcal{L}$	2	2								
H(e,e')										
Normal $\mathcal{L}$	3	3	24	4	4	4	5	6	24	
Half $\mathcal{L}$	3	6	2	2	2	2	2	2	2	
10% $\mathcal{L}$	18	18								
BigBen off	6	6	6	2	2	3	6	6	24	
Dummy target	2	2	2							
H(γ,π^+)										
Radiator	24	24	12							
Dummy target	2	2	2							
No radiator	6	6	3							
Total	106	106	89	42	35	49	118	130	282	$\Rightarrow$ 957
Commissioning										96
3 Energy changes										124
15 angle changes										60
6 polarity changes										24
Beam request										1161 $\approx$48.5 days

Table 12: Estimated contributions (in percent) to errors on R, and resultant errors on G_M^n/G_M^p .

Q^2 (GeV/c)^2	3.5	4.5	6.0	8.5	10.	12.	13.5	16.	18.
proton cross-section	1.7	1.7	1.7	1.7	1.7	1.7	1.7	1.7	4.
G_E^n	1.7	1.1	0.49	0.51	0.56	0.69	0.38	.89	.39
quadrature sum of other syst.	1.72	1.43	1.59	3.4	3.63	3.36	3.85	4.86	4.19
Statistical error	0.3	0.3	0.8	1.4	1.3	2.4	3.2	3.4	5.9
Without proton err.									
Total error on R	2.43	1.83	1.81	3.71	3.89	4.19	5.02	6	7.25
Error on G_M^n/G_M^p	1.22	0.91	0.9	1.85	1.94	2.09	2.51	3	3.62
With proton err.									
Error on G_M^n	1.48	1.25	1.24	2.04	2.12	2.26	2.65	3.12	4.14

Requested beam times are tabulated in Table 11. The first line lists the times, discussed above, found to give a suitable trade-off of statistical and systematic errors. Additional time is requested at lower luminosity to ensure that rate-related effects, such as accidentals, are well understood. At each luminosity, running time on the dummy target is included to ensure that accidental background can be distinguished from target-window background. Time is also requested for calibration of the BigHAND detector with tagged protons and tagged neutrons. In some cases the requested time greatly exceeds the minimum to allow us to take advantage of data which is readily available. The proton calibration rate is so high at the lowest Q^2 points, for example, that adequate statistics could be acquired in a few minutes. This high rate provides an excellent opportunity to study efficiency variation across the face of BigHAND, so far more data taking time is scheduled. Just a few hours of running will give a million events, allowing the BigHAND face to be finely subdivided and precisely calibrated in many separate regions. For several calibration points or high-rate quasi-elastic points we also allow time for running at reduced luminosity to ensure that accidental rates are well understood. Elastic scattering measurements with the 48D48 deflector dipole turned off will be useful for checking the alignment of the $\vec{q}$ inferred from BigBite measurements with the actual hit positions in BigHAND. For the neutron calibration, time is included for running without a radiator to measure the virtual photon contribution. Time is also allowed for running on dummy targets for subtraction of target window contributions. Eight hours are allowed for each beam energy change. In addition to the time required to position the spectrometers for each measurement, each elastic calibration requires two spectrometer-moves and two reversals of the BigBite polarity. Four hours are allowed for each operation. Finally, 72 beam hours are requested for commissioning of the system including the new 48D48 deflector magnet. In total, 28 days are requested.

Figure 24 shows the size of the errors on the extracted values of G_M^n which would be obtained with the desired statistics and the systematic errors given in Table 9 (added in quadrature), see Table 12. The value is arbitrarily plotted at unity. The fractional error on G_M^n has been calculated using the projected error on the proton cross section. Because G_M^n is proportional to $\sqrt{R}$, the error is scaled down by a factor of two to give the fractional error on G_M^n. The errors are seen to be far smaller than those on the few existing data points covering part of this kinematic range.

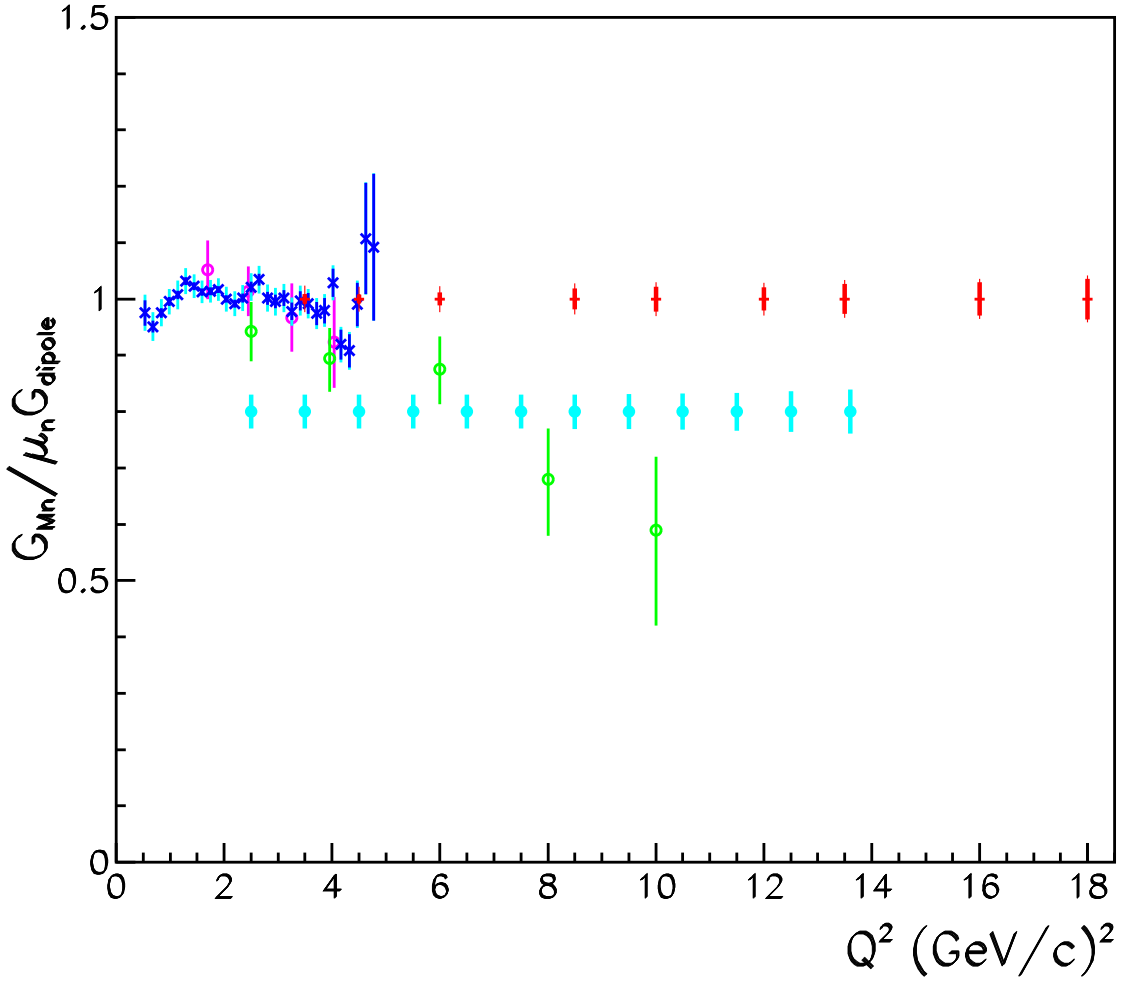

Figure 24: Existing data on G_M^n in the Q^2 range of the proposed measurement are plotted as ratio to scaled dipole approximation. (See caption of Fig. 1.) Red points (arbitrarily plotted at unity) show projected size of error bars for this experiment. Thick error bars include projected statistical and systematic errors of the proposed experiment but do not include errors on other measurements. Thin error bars include statistical and systematic errors and also estimated errors on G_E^n and on the proton elastic cross section. Solid light-blue circles with error bars (arbitrarily plotted at 0.8 for clarity) indicate the position and projected total errors/citeJerry of the CLAS12 experiment.

14 Relation to Other Experiments

This experiment uses much of the same detector equipment as the GEn experiment (E02-013) [43] and many of the collaborators most involved in that experiment are also involved here. Technical expertise in tracking in BigBite and in calibration of BigHAND will be available for this analysis. The large dipole magnet, which is proposed for deflection of protons, is a part of an approved 12 GeV experiment which will measure Electric Form Factor of the proton at very large Q^2 [56].

High precision measurements of the neutron magnetic form factor were made at lower Q^2 in the CLAS e5 measurement (E94-017). Many of the principle people involved in the analysis [39] of that data set are involved in the present proposal. This measurement will complement the CLAS measurement by extending the precision measurements to a far higher Q^2. We will draw on much expertise and experience in controlling systematic errors in such a ratio measurement.

A 12 GeV experiment (E12-07-104) has been approved to extend the high-precision measurements of G_M^n out to beyond $Q^2 = 13$ $(GeV/c)^2$ using the CLAS12 detector. Some of the spokespersons of that experiment are also involved in the present proposal. The results from the two experiments will be complementary in that the CLAS12 data will have generally larger systematic errors (3% estimated systematic error on G_M^n) [57] but will cover a subset of the range of Q^2 (up to about 14 $(GeV/c)^2$) with contiguous coverage which can be subdivided into many data points. The proposed experiment would measure nine discreet Q^2 values and extend the coverage $Q^2 = 18$ $(GeV/c)^2$). The present proposal aims to have significantly smaller systematic errors (and for high Q^2 points, smaller statistical errors) in the region of overlap. CLAS12 is a large-acceptance device which, by its nature, collects data simultaneously at many scattering angles but with low luminosity. The proposed experiment collects data only at predetermined angles but can run at far higher luminosity (the planned luminosity for this proposal is over 600 times the design luminosity for CLAS12). Systematic errors are more easily controlled for single-position detectors than for large acceptance detectors. The use of the same detector for both nucleon species also helps control the systematic errors in the proposed measurement. In the present proposal, the large baseline between the target and the hadron detector (17 m) also provides a major advantage in selection of quasi-elastic events due to superior angular and momentum resolution.

Since neutron-detection statistics dominate the statistical errors, Table 13 compares the expected statistics of Quasi-elastic neutrons detected in each experiment. Because of the CLAS12 measurements are all made simultaneously, the statistics fall off rapidly at high Q^2. In the present experiment the high luminosity can be combined with beam times tailored to each kinematic point to make the statistics more even. It is seen that the present experiment not only extends the coverage to higher Q^2 than the CLAS12 experiment, but also beyond $Q^2 = 10$ $(GeV/c)^2$ it has significantly higher statistics.

Our experience on the CLAS e5 experiment showed it to be very valuable to have overlapping measurements. There, two beam energies and two neutron detection systems allowed up to four redundant measurements in some regions. This was beneficial as a way to protect against unsuspected systematic problems in each of the measurements. Ultimately each of the experiments will benefit from the partial overlap of the kinematic coverage. The CLAS12 data will serve as a useful check of the lower-Q^2 results of the present proposal. Inspection of the existing data (Fig. 24) suggests that the proposed measurement must either see an abrupt change in the behavior of the form factor in this kinematic range or be in conflict with either the CLAS [39] or SLAC [26] data sets. In any of those cases, the CLAS12 data would then be an important confirmation.

Table 13: Comparison of expected statistics of detected neutrons between CLAS12 experiment and present proposal. Dashes indicate points beyond the kinematic range of an experiment, asterisks indicate points for which no measurement is made. The last column lists the time allocated for data-taking in the present experiment. This may be compared to the total or 56 days (1344 hours) over which the CLAS12 experiment would acquire the statistics given in column 2.

Q^2 $(GeV/c)^2$	CLAS12	Present proposal	Hours
2.5	1.6×10^5	—	
3.5	2.3×10^6	2.1×10^5	12
4.5	6.6×10^5	1.4×10^5	12
5.5	89000	*	
6.0	*	28000	18
6.5	35000	*	
7.5	16000	*	
8.5	7700	11300	18
9.5	4000	*	
10	*	13900	24
10.5	2200	*	
11.5	1300	*	
12	*	4100	36
12.5	800	*	
13.5	500	2550	96
16	—	2380	108
18	—	800	216

15 Group Contributions to 12 GeV Upgrade

The following is a list of personnel from the institutions and their intended contribution to the proposed experiment:

- The CMU spokesperson and collaborators have long experience with neutron detectors and recent experience with the BigHAND detector (which includes 100 scintillator detectors provided by CMU). This group will perform the work necessary to prepare the BigHAND detector and to ensure that its elements and readout are ready for operation.
- The Hall A spokesperson and collaborators will be responsible for infrastructure of the 48D48 magnet, which is a part of three Form Factor experiments.
- The Rutgers spokesperson and collaborators will be responsible for preparation of the data acquisition components including front-end electronics and customized software.

In addition to equipment specific to this experiment, many collaborators are involved in projects in support of equipment for use in Hall A in the 12 GeV era. Many of these components are parts of the Super BigBite spectrometer (SBS) which will use the BigBen spectrometer and GEM detectors, among other components.

- The INFN collaborators of are committed to provide a reconfigured tracker in BigBite and its operational support. They will also have a major role in implementation of the RICH in Hall A. The source of funding for this group is INFN. INFN has approved about $150k for prototyping of the large GEM chambers and expected to support whole front tracker in GEP5 experiment including electronics for high resolution operation in SBS and BB.
- The UVA collaborators are responsible for construction and operation of high polarization high luminosity He target, which is a major part of the new GEN proposal to this PAC. The UVA collaborators are also responsible for reconfiguration of the tracker in the Super BigBite Spectrometer and its operation. The source of funding for this group is DOE. The University of Virginia group, which recently developed a major new tracker for the BigBite spectrometer, will submit an MRI proposal to NSF for construction of a GEM-based tracker for SBS.
- The Glasgow group intends to work on GEM-based detectors for the PANDA experiment and will share their results in hardware design and readout software with this effort, effectively contributing several FTE's.
- The Florida International University also intends to contribute in the development of a GEM-based tracker at least 1 FTE and put a graduate PhD thesis student in this experiment.
- The CMU group will use their expertise to implement the hadron calorimeter and the beam line magnetic shielding, both of which also required in the GEP5 experiment E12-07-109. This group has also become involved in the development of Compton polarimeter equipment for Hall A, and will continue that development into the 12 GeV era. The source of funding for this group is DOE.

- Along with the CMU group, College of William and Mary group, together with Dubna collaborators, intends to prepare the hadron calorimeter elements and their implementation in time for the experiment around 2014.

References

[1] M.N. Rosenbluth, Phys. Rev. **79** 615 (1950).

[2] M.K. Jones *et al.*, Phys. Rev. Lett.**84** 1398 (2000).

[3] O. Gayou *et al.*, Phys. Rev. Lett.**88** 092301 (2002).

[4] A.V. Afanansev *et al.*, Phys. Rev. D **72** 013008 (2005).

[5] G. Miller, Phys. Rev. Lett. **99** 112001 (2007).

[6] D. Kaplan and A. V. Manohar, Nucl. Phys. B **310**, 527 (1988).

[7] R. D. McKeown, Phys. Lett. B **219**, 140 (1989).

[8] D.H. Beck, Phys. Rev. D **39**, 3248 (1989).

[9] D. Müller, D. Robaschik, B. Geyer, F.M. Dittes, J. Horejsi, Fortsch. Phys. 42 (1994) 101.

[10] X. Ji, Phys. Rev. Lett. **78**, 610 (1997); Phys. Rev. D **55**, 7114 (1997).

[11] A.V. Radyushkin, Phys. Lett. B **380**, 417 (1996); Phys. Lett. B **385**, 333 (1996); Phys. Rev. D **56**, 5524 (1997).

[12] T. Eden *et al.*, Phys. Rev. C **50**, R1749 (1994).

[13] M. Ostrick *et al.*, Phys. Rev. Lett. **83**, 276 (1999).

[14] C. Herberg *et al.*, Eur. Phys. Jour. A **5**, 131 (1999).

[15] Jefferson Lab experiment E93-038, spokespersons: R. Madey, S. Kowalski.

[16] I. Passchier *et al.*, Phys. Rev. Lett. **82**, 4988 (1999).

[17] H. Zhu *et al.*, Phys. Rev. Lett. **87**, 081801, 2001.

[18] M. Meyerhoff *et al.*, Phys. Lett. B **327**, 201 (1994).

[19] H. Gao *et al.*, Phys. Rev. C **50**, R546 (1994); H. Gao, Nucl. Phys. A **631**, 170c (1998).

[20] W. Xu *et al.*, Phys. Rev. Lett. **85**, 2900 (2000).

[21] W. Xu *et al.*, Phys. Rev. C. **67**, R012201 (2003).

[22] E.B. Hughes *et al.*, Phys. Rev. **139**, B458 (1965); *ibid.* **146**, 973 (1966).

[23] B. Grossetête, S. Jullian, and P. Lehmann, Phys. Rev. **141**, 1435 (1966).

[24] A.S. Esaulov *et al.*, Sov. J. Nucl. Phys. **45**, 258 (1987).

[25] R.G. Arnold *et al.*, Phys. Rev. Lett. **61**, 806 (1988).

[26] S. Rock *et. al.*, Phys. Rev. D **46** 24 (1992).

[27] A. Lung *et al.*, Phys. Rev. Lett. **70**, 718 (1993).

[28] R.J. Budnitz *et al.*, Phys. Rev. **173**, 1357 (1968).

[29] K.M. Hanson *et al.*, Phys. Rev. D **8**, 753 (1973).

[30] P. Stein *et al.*, Phys. Rev. Lett. **16**, 592 (1966).

[31] W. Bartel *et al.*, Phys. Lett. B **30**, 285 (1969); *ibid.* **39**, 407 (1972); Nucl. Phys. B **58**, 429 (1973).

[32] P. Markowitz *et al.*, Phys. Rev. C **48**, R5 (1993).

[33] H. Anklin *et al.*, Phys. Lett. B **336**, 313 (1994).

[34] E.E.W. Bruins *et al.*, Phys. Rev. Lett. **75**, 21 (1995).

[35] H. Anklin *et al.*, Phys. Lett. **B428**, 248 (1998).

[36] G. Kubon *et al.*, Phys. Lett. **B524** 26 (2002).

[37] J. Lachniet et al, nucl-ex 0811.1716, submitted to Phys. Rev. Lett.
JLab Experiment E94-071
"The Neutron Magnetic Form Factor from Precision Measurements of the Ratio of Quasielastic Electron-Neutron to Electron-Proton Scattering in Deuterium", W. Brooks and M. Vineyard spokespersons.

[38] L. Durand, Phys. Rev. **115** 1020 (1959).

[39] J, Lachniet thesis, Carnegie Mellon University, unpublished, June, 2005
http://www-meg.phys.cmu.edu/ bquinn/jeff_thesis.pdf

[40] "Measurement of the Neutron Electromagnetic Form Factor Ratio GEn/GMn at High Q2" proposal to PAC34, S. Riordan, G. Cates and B.Wojtsekhowski (spokespersons).

[41] H. Arenhövel, private communication.

[42] S. Jeschonnek and J.W. Van Orden, Phys. Rev. C, **62** 044613, 2000.

[43] JLab experiment E02-013, G.Cates, N.Liyanage and B.Wojtsekhowski (spokespersons).

[44] S.Riordan, private communication.

[45] See proposal of JLab Experiment E12-06-122 "Measurement of neutron asymmetry A_1^n in the valence quark region using BigBite spectrometer." G.Cates, N.Liyanage , Z.Meziani, G.Rosner, X.Zheng and B.Wojtsekhowski (spokespersons).

[46] Rob Feuerbach, private communication.

[47] S.Abrahamyan, GEANT-4 simulation with saturation effect in light output.

[48] J.L. Matthews and R.O. Owens, Nucl. Instr. and Meth. **111**, 157 (1973).

[49] E.L. Lomon and H. Feshbach, Annals of Phys. **48** 94 (1968).

[50] E12-07-108 proposal.

[51] Data from PDG, http://pdg.lbl.gov/xsect/contents.html and references therein.

[52] M.Ripani and E.M.Golovach based on P.Corvisiero, *et al.*, Nucl. Instr. and Meth. A, **3464** 33 (1994).

[53] L.M. Stuart, *et. al.*, Phys. Rev. D **58** 032003 (1998).

[54] L.Y. Zhu, *et. al.*, Phys. Rev. C **71** 044603 (2005).

[55] R.L. Anderson, *et al*, Phys. Rev. D **14** 679 (1976).

[56] JLab E12-07-109, Ch. Perdrisat *et al*, Large Acceptance Proton Form Factor Ratio Measurements at 12 and 15 $(\mathrm{GeV}/c)^2$ Using Recoil Polarization Method.

[57] G. Gilfoyle, private communication.